Thesis

A Simplified Model for Understanding
Natural Convection Driven Biomass Cooking Stoves

Submitted By

Joshua Nicholas Agenbroad

Department of Mechanical Engineering

In partial fulfillment of the requirements

For the Degree of Master of Science

Colorado State University

Fort Collins, Colorado

Summer 2010

Colorado State University

June 28, 2010

We Hereby Recommend That The Thesis Prepared Under Our Supervision By Joshua Nicholas Agenbroad Entitled A Simplified Model for Understanding Natural Convection Driven Biomass Cooking Stoves Be Accepted As Fulfilling In Part Requirements For The Degree Of Master Of Science.

Committee on Graduate Work

Allan T. Kirkpatrick

Eric D. Maloney

Advisor: Morgan Defoort

Co-Advisor: Bryan D. Willson

Department Head: Allan T. Kirkpatrick

Abstract of Thesis

A Simplified Model for Understanding
Natural Convection Driven Biomass Cooking Stoves

It is estimated that half the world's population cooks over an open biomass fire;
improved biomass cooking stove programs have the potential to impact indoor air
quality, deforestation, climate change, and quality of life on a global scale. The ma-
jority of these cooking stoves operate in a natural convection mode (being driven by
chimney effect buoyant fluid forces). Simplified theories for understanding the behav-
ior of this unexpectedly complex combustion system, along with practical engineering
tools to inform its design are markedly lacking. A simplified model of the fundamen-
tal stove flow physics is developed for predicting bulk flow rate, temperature, and
excess air ratio based on stove geometry (chimney height, chimney area, viscous and
heat release losses) and the firepower (as established by the stove operator). These
parameters are intended to be fundamental inputs for future work understanding and
improving biomass cook stove emissions and heat transfer.

Experimental validation is performed and the simplified model is shown to be both
accurate and applicable to typical stove operation. Carbon monoxide and particulate
matter emissions data has been recorded in conjunction with the validation data. The
initial results are presented and indicate that the excess air ratio may be a promising
tool for reducing carbon monoxide emissions.

A dimensionless form of the simplified stove flow model is then developed. This
form offers several advantages, including scale similarity and a reduction of indepen-
dent experimental parameters. Plotting with dimensionless parameters, various stove

configurations can be plotted concurrently, and general stove flow behavior common to all natural convection stoves is observed. With a dimensionless firepower axis, emissions trends for both carbon monoxide and particulate matter become apparent, and a region of improved combustion efficiency and lowered emissions is identified.

Joshua Nicholas Agenbroad
Department of Mechanical Engineering
Colorado State University
Fort Collins, CO 80523
Summer 2010

Contents

List of Figures

List of Tables

1 Introduction

It is estimated that about half the world's population, more than 3 billion people, cook over an open biomass fire. This energy source is especially prevalent in rural areas of developing countries, where an estimated 90% of households rely on biomass fuels for cooking [8]. Despite being a simple, convenient, and potentially carbon neutral energy source, several important challenges are apparent:

1.1 Indoor Air Quality

Combustion of solid biomass fuel is especially prone to incomplete combustion often resulting in harmful emissions. These emissions, when combined with poor ventilation, often lead to poor indoor air quality and a number of adverse health effects. Harmful emissions include primarily particulate matter and carbon monoxide (CO), but also inorganic gases (nitric and sulfur oxides, ozone, etc), hydrocarbons (polycyclic and mono aromatics, etc), oxygenatated organics, chlorinated organics, and free radicals [8, 19].

Raub and Benignus [21] provide a good review of carbon monoxide exposure health effects. Carbon monoxide enters the body through the lungs and attaches to hemoglobin oxygen carriers in the blood, thereby preventing the intended oxygen uptake. The body's organs and tissues become oxygen starved. High exposure can be deadly. More commonly, acute exposure can lead to dizziness, weakness, nausea, vomiting, disorientation, confusion, collapse, and coma. Chronic symptoms are also being identified.

Particulate matter (PM) inhalation has been linked to five major categories of illness. These include chronic obstructive pulmonary disease (COPD), heart disease, cancer, acute respiratory infection (mainly with children), and low birth weights [8].

For an extensive review of the mechanisms and exposure concerns, see Naeher et al. [19], Directors and Senior Associates of the PM Centers Headquartered at UCLA [9].

The remaining emissions are not necessarily less important, but difficult to measure and understand. These inorganic gases, hydrocarbons, oxygenatated organics, chlorinated organics, and free radicals are known to include carcinogens, irritants, mutagens, and neurotoxins, as discussed in an extensive review by Naeher et al. [19].

Over 1.6 million deaths a year are attributed to poor indoor air quality as a result of domestic biomass combustion products, accounting for about 3% of the global health burden [29]. Women and children are affected disproportionately due to higher exposure and lowered immunity. Poor indoor air quality is thought to be the leading cause of death worldwide for children under the age of five [4].

1.2 Deforestation and Climate Change

Beyond the direct exposure health concerns, cooking with biomass fuel can also have important global implications on greenhouse gas and black carbon emissions. Smith [27] and Haines et al. [12] provide a good discussion of the overall global warming potential; cooking with biomass fuels is thought to account for 1-3% of all human generated global warming. In Venkataraman et al. [31], biomass cooking is suggested to be the dominant source of global black carbon emissions. Biomass cooking is also a significant source of deforestation and consequent climate forcing as discussed in Mwampamba [18]. For many of the world's poorest groups, acquiring biomass fuel also presents a heavy burden of time and/or money.

1.3 Performance Goals

With these issues in consideration, major stove metrics can be summarized as follows:

- Reducing harmful emissions due to products of incomplete combustion.

- Increasing thermal efficiency, thus reducing fuel consumption.

1.4 Improved Cook Stoves

Biomass fueled cook stove technology is increasingly being used to address these performance goals [3, 1]. The "three stone fire" is the most basic, but still extremely common, method for cooking with biomass fuel, and is often used as a benchmark for comparison. The three stone fire is simply an open fire, gaining its name from the stones used to hold the cook piece over the fire. Improved biomass cook stoves have been able to reduce CO and PM emissions by 50-75% and increase fuel efficiency by 30-50% compared to the three stone fire configuration [15]. These reductions are accomplished largely by enclosing the fire in a combustion chamber. The primary benefits of chamber enclosure are airflow control (providing better mixing with reduced quenching) and reduced radiative and convective heat transfer losses. The combustion chamber also allows the stove designer to locate the cook piece for increased heat transfer and reduced emissions. One such stove, the well known "rocket elbow" design, shown in Figure 1, will be utilized for this research.

The present research will be performed entirely with wood fuel. 32% of the worlds population has been reported to rely principly on wood fuel; this number increases to 45% in the developing world, where wood in the most common utilized fuel choice [8]. In Smith et al. [28], the "energy ladder" is described, wherin more developed groups with higher incomes move up the energy ladder using fuels with lower harmful emmissions. Wood fuel ranks near the middle of this energy ladder.

While the development of this research has utilized a wood burning "rocket elbow" stove, the results are likely applicable to other stove/fuel configurations, perhaps modified or extended slightly.

Figure 1: Insulated Rocket Elbow Stove.

1.5   Stove Design and Model Motivation

There exists a wide variety of improved stove designs with varying performance [26]. Stove efficiency and emissions are very sensitive to the combustion chamber shape, material, chimney height, chimney diameter, and cook piece placement. These design choices have been studied by improved cook stove projects for over 40 years. A great deal has been learned, resulting in many empirically/observationally established design guidelines, but rarely in theory based analytical or numerical design tools [26]. The rocket elbow stove design used in this research is a good example. The design has been empirically studied and refined for at least two decades, and the resulting design guidelines have been documented [2, 14, 25, 5]. Moving beyond this kind of empirical/observational approach, the complexity of the physical and chemical processes, as well as their interconnection, increases rapidly.

For the development of basic analytical theory and practical engineering tools, it becomes necessary to extract the simplified fundamental processes governing basic stove behavior. In the field of biomass cooking stoves research, this type of simplified, foundational theory is notably lacking.

1.6 The Simplified Stove Flow Model

A simplified model of the essential stove flow physics will be developed in this thesis for predicting bulk flow rate, temperature, and excess air ratio based on stove geometry (including chimney height, chimney area, viscous and heat release losses), and the operating firepower. Stove geometry inputs are of interest to the stove designer as they are basic tools for influencing stove performance. The stove firepower is primarily established by the operator, and is consequently included as a model input as well.

The resulting bulk flow rate, temperature, and excess air ratio behavior are intended to provide insight and fundamental inputs for beginning to understand, model, and improve stove performance. Bulk flow rate and temperature are important inputs for analytical, empirical, and numerical studies of heat transfer and stove emissions. A simplified model is also conducive to use in optimization and automated routines.

Although excess air ratio is most traditionally applied to premixed combustion, it has also been applied to biomass boiler design and operation for affecting emissions (primarily carbon monoxide). Initial results included here will suggest its suitability for biomass cook stove design; excess air ratio appears to be a promising tool in predicting and affecting carbon monoxide emissions. Excess air ratio will also be used to understand a stove's firepower range, within which the operator will determine the firepower.

The fundamental physics of the simplified stove flow model will first be validated using two rocket elbow geometries without a cook piece in place. The relative importance of the initially unknown and complex viscous and heat transfer losses is greatly increased with the cook piece in place. The without cook piece configuration is used to test baseline model accuracy for a somewhat idealized case. Analogous validation data will then be taken with the cook piece in place to study the validated stove flow model's application and practical implementation.

A dimensionless form of the simplified stove flow model is also developed. This form will reduce stove behavior to a general and fundamental form independent of geometry. The model solution is no longer specific to stove configuration geometry, and the single solution can be used to lookup stove behavior for various stove geometries. The dimensionless form also provides a reduction of independent experimental parameters allowing the comparison of results for all stove configurations.

Observed emissions trends will be shown to be even more convincing when plotted in dimensionless form. Carbon monoxide and particulate matter emissions results for the various validation configurations are plotted together with dimensionless firepower. With the dimensionless axis, both carbon monoxide and particulate matter emissions trends are observed, and a region of improved combustion efficiency (with reduced harmful emissions) is suggested. With these interesting results, overall model conclusions are discussed, and the case is made for further research.

2 Model Setup

A schematic setup of the analytical stove flow model to be developed is shown in Figure 2. The 1-D flow shown in Figure 2 is assumed. The physics of the stove have been simplified to two basic and fundamental driving processes: heat addition from combustion (at point 2), and kinetic energy addition/conversion (between points 1 and 2) due to the chimney effect. The two processes are interconnected and together govern the simplified overall stove operation.
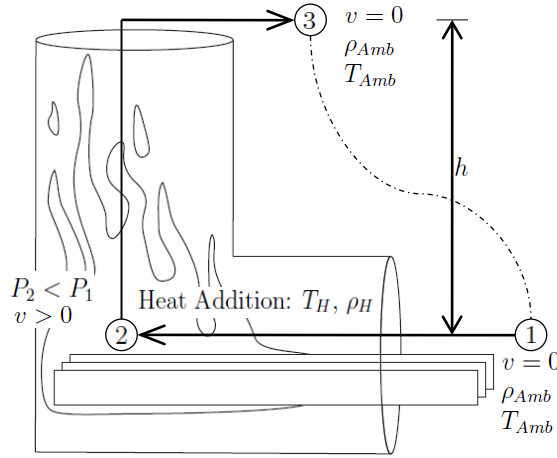
Figure 2: Simplified model setup.

2.1 Heat Addition

The driving fire releases heat into the passing stove flow, increasing its temperature and decreasing its density. Heat addition is assumed to be perfectly efficient and is greatly simplified as taking place entirely, instantaneously, and uniformly at point 2. For a given mass flow rate, $\dot{m}_A$, and heat release rate (essentially the current stove firepower), $\dot{Q}_{in}$, the bulk flow temperature increase can be calculated using the first law of thermodynamics for a control volume.

For an isobaric system with no mechanical work, assuming ideal gas behavior, and constant potential and kinetic energy, the temperature increase can be calculated us-

ing the constant pressure specific heat of air (c_p). The heat addition from combustion translates into an enthalpy (h) increase distributed over the mass flow rate ($\dot{m}_A$) as shown in Eq. (1).

$$
\begin{aligned}
\dot{Q}_{cv} &= \dot{m}_A(h_{Amb} - h_H) \\
&= \dot{m}_A \int_{T_{Amb}}^{T_H} c_p(T)dT \\
&= \dot{m}_A c_{p,avg}(T_H - T_{Amb})
\end{aligned}
\tag{1}
$$

Where T is the bulk flow temperature, and the subscripts H and Amb denote hot and ambient (cold) respectively. A constant specific heat, evaluated at an average temperature will be assumed. Heating takes place over a range from approximately 300-1300K, over which specific heat varies by a maximum of 15%. Specific heat can also be calculated using a piecewise polynomial of the form described in Kee et al. [16], the resulting error never exceeds 2%, and is considered negligible. For details see Appendix A.

2.2 Chimney Effect

Airflow through the stove is dependent on the chimney effect resulting from the buoyant force of the decreased density air after combustion heat addition. The chimney effect equation will be briefly derived. The decreased density air in the chimney between points (2) and (3) creates a lowered pressure at point (2) compared to the ambient pressure at point (3). In a fluid, pressure increases with depth, and the pressure increase (ΔP) can be calculated using the hydrostatic equation, given below in Eq. (2).

$$\Delta P = g \int \rho(h)dh \tag{2}$$

Where g is gravity, and the density (ρ) is a function of chimney height (h). The pressure at points (1) and (2) can be calculated using Eq. (2), the former by starting at point (3), and integrating while traveling down the chimney to point (2), and the latter by traveling outside of the chimney through ambient air (with constant ambient density (ρ_{Amb}) to point (1). The difference is found by subtracting the two results, as shown in Eq. (3).

$$
\begin{aligned}
\Delta P_{1-2} &= \left(P_3 + g \int_3^1 \rho_{Amb}dh\right) \\
&\quad - \left(P_3 + g \int_3^2 \rho(h)dh\right) \\
&= g\rho_{Amb}h - g \int_3^2 \rho(h)dh
\end{aligned}
\tag{3}
$$

If we assume the chimney walls to be adiabatic, than the temperature and density of the gas in the chimney (T_H and ρ_H) will remain constant, and Eq. (3) simplifies to Eq. (4).

$$\Delta P_{1-2} = gh(\rho_{Amb} - \rho_H) \tag{4}$$

In reality, approximately one third of the energy may be lost to the chimney walls. In this case the integral from point (2) to (3) could be performed if the temperature/density profiles were known. For the simple model presented here, no attempt is made to calculate these profiles, and the adiabatic chimney assumption is maintained.

Chimney flow results from the pressure difference calculated in Eq. (4); the gain in kinetic energy of the chimney flow at point (2) from the stagnant ambient air at point (1) is equated to this pressure difference using the integral form of Bernoulli's equation for compressible flow, as shown in Eq. (5).

$$
\begin{aligned}
\Delta P_{1-2} &= gh(\rho_{Amb} - \rho_H) \\
&= \frac{1}{2}\rho_H v_2^2
\end{aligned}
\tag{5}
$$

Where the hot gas density and velocity (v) at point (2) are used for calculating the stove flow kinetic energy. Velocity, volume $(\dot{V})$ and mass air flow $(\dot{m}_A)$ rates are related by the flow area (A) and density. Again assuming ideal gas behavior, the density is related to the temperature by the ideal gas law. Utilizing these relations and solving Eq. (5) for volume and mass flow rate (Detailed in Appendix B) yields Eq. (6)-(9). Eq. (8) is the commonly known form of the chimney effect equation. The mass flow rate form shown in Eq. (9), will be a more applicable and interesting form for the purposes of this paper.

$$
(\rho_{Amb} - \rho_H)gh = \frac{1}{2}(\rho_H)\left(\frac{\dot{V}}{A}\right)^2
\tag{6}
$$

$$
\dot{V} = CA\sqrt{2gh\left(\frac{\rho_{Amb} - \rho_H}{\rho_H}\right)}
\tag{7}
$$

$$
\dot{V} = CA\sqrt{2gh\left(\frac{T_H - T_{Amb}}{T_{Amb}}\right)}
\tag{8}
$$

$$\dot{m}_A = CA\left(\frac{P}{R_s}\right)\left(\frac{1}{T_H}\right)\sqrt{2gh\left(\frac{T_H - T_{Amb}}{T_{Amb}}\right)} \tag{9}$$

Where C is a loss coefficient introduced to account for uncertainties and inefficiencies in the chimney effect, primarily including viscous losses, chimney wall heat transfer, and the unrealistic ideal point heat addition at point two.

2.3 The Loss Coefficient

In reality heat is released throughout the chimney at the flame; when this heat addition takes place after point two, the chimney density profile used in Eq. (3) and (4) is less effective in producing the chimney effect in Eq. (8) and (9). In this case, as well as with chimney wall heat losses, the result is a reduced chimney effect and $0 \leq C \leq 1$. Viscous losses due to friction and geometric restriction are included here as well. The loss coefficient magnitude and dependence will be discussed further in Chapter 6, but will initially be assumed constant.

2.4 Combine and Solve, Inputs and Outputs

Solving Eq. (1) and (9) simultaneously a simple model for predicting stove bulk flow and temperature is determined. The system of equations is shown in Figure 3, along with the input, output, and feedback connection between the combustion heat addition and the chimney effect flow. Stove geometry and firepower are included as inputs as previously discussed.

The two equations can be solved iteratively, in this case using a MATLAB® script (included in Appendix C). The iterative solution results in a steady state bulk flow
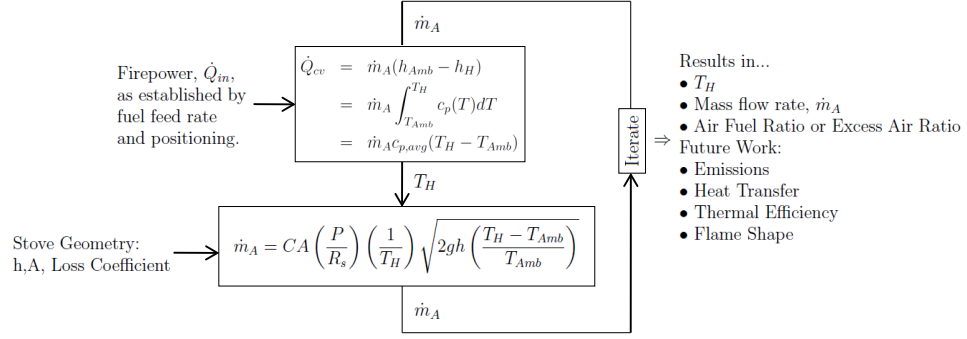
Figure 3: Overall system of equations w/ inputs and outputs.

rate and temperature for a given stove geometry and operating firepower/fuel feed rate. Although the actual stove behavior is inherently transient, these steady state values will be shown to have physical significance for temporally averaged behavior.

The air/fuel ratio (AFR) and a bulk excess air ratio (EAR) can be calculated using the chimney effect driven mass flow rate and the fuel mass burn rate. The mass flow rate of fuel ($\dot{m}_F$) is calculated from the firepower ($\dot{Q}_{in}$) and the heating value (HV) of the fuel as shown in Eq. (10). The AFR and EAR can then be calculated as shown in Eq. (11)-(13), where AFR_{stoich} is the AFR for stoichiometric combustion.

$$\dot{m}_F = \frac{\dot{Q}_{in}}{HV} \tag{10}$$

$$AFR = \frac{\dot{m}_A}{\dot{m}_F} \tag{11}$$

$$\Phi = \frac{AFR_{stoich}}{AFR} \tag{12}$$

$$\%EAR = \frac{(1 - \Phi) \cdot 100\%}{\Phi} \tag{13}$$

12

The lower or the gross heating value (LHV or GHV) is used (where the LHV is essentially the heat of combustion). However, the higher heating value (HHV) should not be used as the latent heat of the water vapor is significant and will not be recovered, either in the chimney flow or by the cook piece. The GHV accounts for the moisture content of the fuel, and the heat that must be consumed for vaporization during pyrolysis. To be even more complete, this vapor must also be raised to the temperature of the chimney gases. Including these effects, error is found be to no more than 3% and are deemed negligible, as determined in Appendix A.

3   Model Results and Discussion

The system of equations described above has been solved iteratively over a typical range of operating firepowers and the results are shown in Figures 4-6. Rocket elbow stove geometry used is given in Table 1. A LHV of 18.280MJ/kg and a $C_{4.4}H_{6.3}O_{2.5}$ fuel composition (ultimate analysis taken from Tillman [30] for Douglas Fir) were used.

3.1   Flow Rate and Temperature Results

Bulk flow temperature, volumetric and mass flow rate behavior are shown for varying firepower in Figure 4. Heat transfer and viscous losses are neglected at this point and the loss coefficient was is equal to one. Volume flow rate and temperature are as expected; increasing firepower leads to increasing flow rate and temperature. Mass flow rate behavior is more interesting; a peak mass flow rate is observed at a relatively low firepower, after which mass flow rate decreases with increasing firepower. The increasing volumetric flow rate is essentially competing with the decreasing flow density due to the increasing flow temperature.

3.2   Excess Air Ratio Results

As firepower is increased, this peak and the following reduction in oxidizer flow rate, have an interesting effect on stove excess air ratio behavior. Excess air ratio (as

	4in. RE	5in.RE
Total height	250mm	320mm
Chimney height	200mm	255mm
Chimney diameter	100mm	130mm

Table 1: Stove Geometry Parameters.
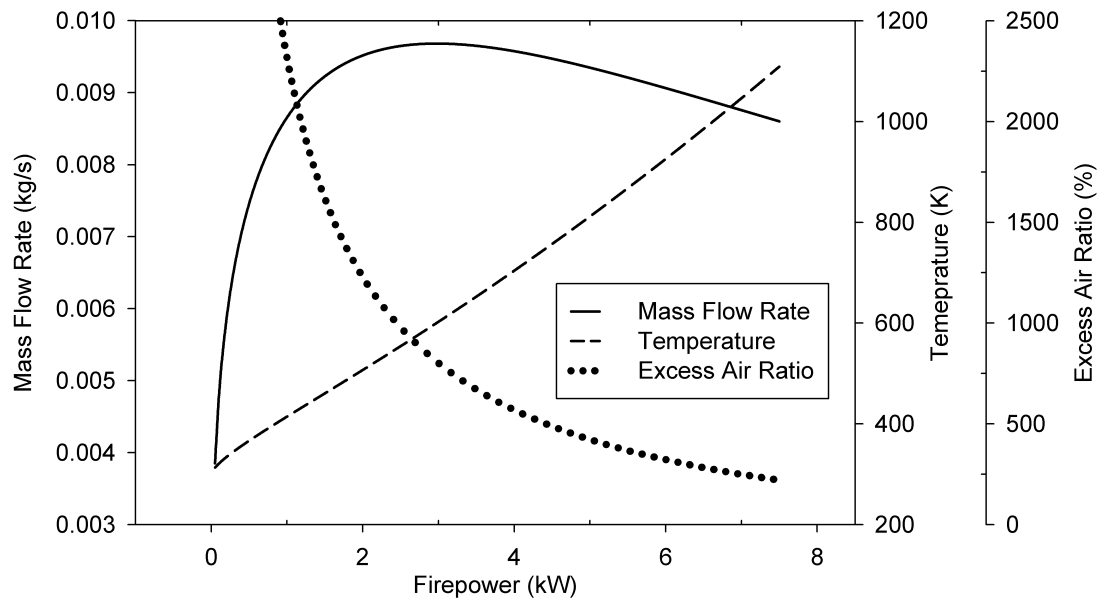
Figure 4: Volume flow rate, temperature and excess air ratio behavior
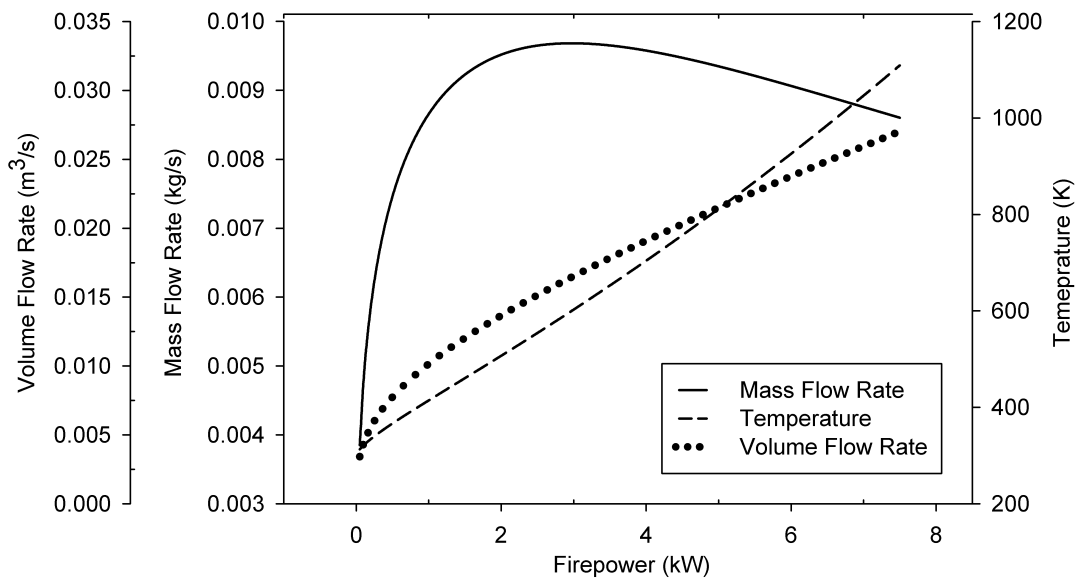
Figure 5: Mass flow rate, temperature and excess air ratio behavior.
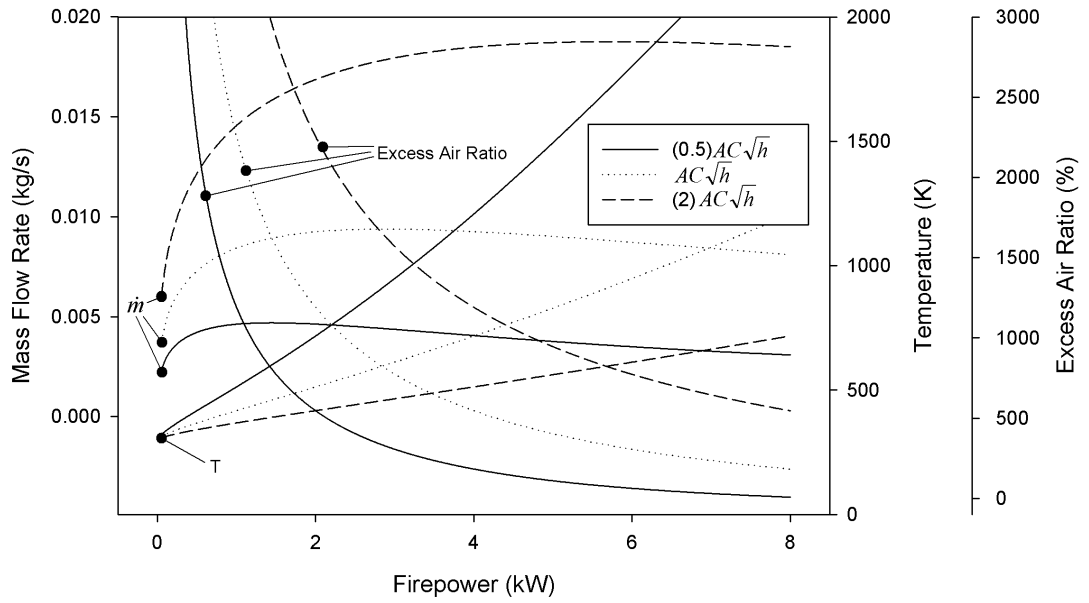
Figure 6: Effect of varying stove geometry parameters.

calculated from Eq. (13)) is shown with temperature and mass flow rate behavior in Figure 5. The excess air ratio is very large while operating at low firepowers, but decreases rapidly, approaching 0% as firepower is increased across the typical stove operating range.

As very low excess air ratios are approached, a theoretical upper limit of firepower (the stove's maximum firepower) is predicted at 0% excess air ratio. At this point exactly sufficient oxidizer is supplied for combustion of the current fuel supply rate. A further increase (assuming no limit in pyrolysis fuel supply is reached first) will not have sufficient oxygen for combustion, and a corresponding increase in stove firepower output cannot be achieved. Considering the poor mixing of actual stove operation, this limit will likely be reached at some point before 0% excess air ratio.

At low firepower, predicted high excess air ratios lead to quenching and cooler temperatures, which likely promote incomplete combustion and a reduction in thermal efficiency. However it not expected that high excess air ratios limit a minimum

16

firepower. For example, in the "three stone fire," excess air ratios would be considered to be very large, if not infinite, for the entire range of operation.

3.3 Geometry Effects

Finally we look at the effect of varying geometry inputs. The three geometry inputs appear together in Eq. (9); their effect can be summarized by their product $CA\sqrt{h}$. The effect of doubling and halving the product of this group is shown in Figure 6.

4   Experimental Validation Setup

Experimental validation has been performed using two sizes of the standard rocket elbow geometry, fed by hand with wooden stick fuel for temporally averaged data sampling.

Operation is similar to actual use, thus assessing the model's practical applicability, but requiring temporal averaging due to its inherently transient nature. A "test sweep" is performed consisting of a sweep through five target firepowers. Firepower is held as constant as possible for each of the five, 15 minute long, sampling periods. These 15 minute sampling periods are then temporally averaged for values of each measured parameter. Firepower is controlled by varying fuel feed rate, number of sticks, and stick positioning. A 15 minute transient period is allowed between data sampling periods for the stove to adjust to each new firepower. The rocket elbow's low thermal mass and the fiberfrax insulation also help minimize transient effects. An example of the raw data collected for one test sweep is shown in Figure 7, with the warm-up, sampling, and transient periods shown.

Two stove sizes (of the dimensions given in Table 1) are used to test the model's accuracy for varying geometry. Two test sweeps are performed for each stove geometry. Validation is for the somewhat idealized case without a cook piece in place, minimizing unknown flow restriction, heat loss effects, and assessing baseline model accuracy. Practical model validation for the case with a cook piece in place will be studied in Chapter 8.

By measuring stack exhaust temperature and $\%O_2$ along with mass based stove emissions of CO and CO_2, the firepower, mass flow rate and temperature are determined for comparison to the model predicted behavior.
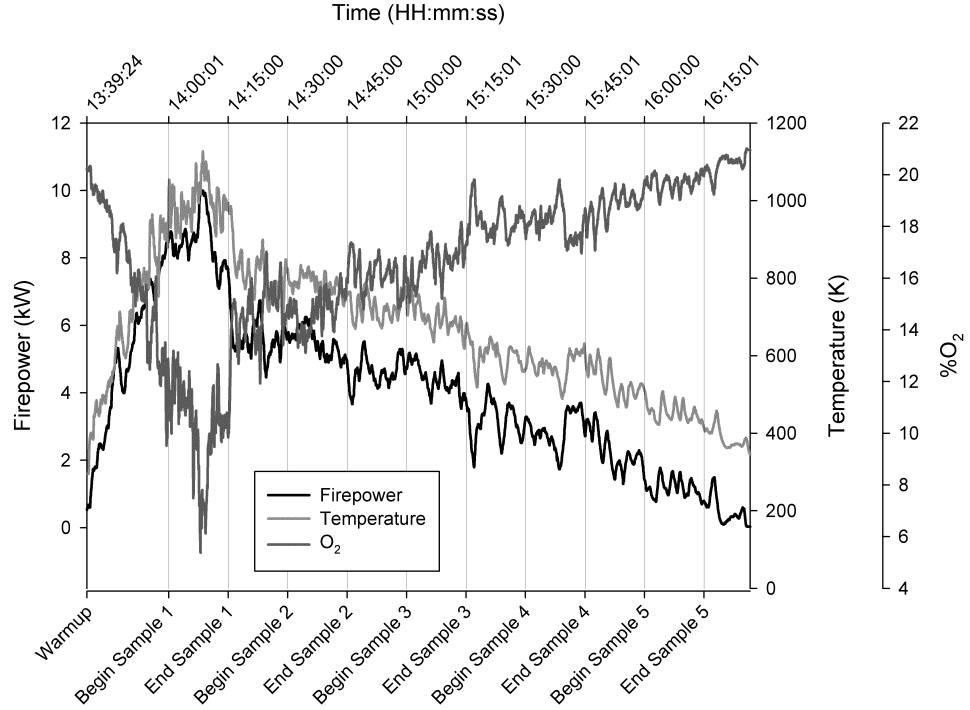
Figure 7: Example raw data before temporal averaging from 4in. RE Test 1.

4.1 Measuring Firepower

Firepower is determined using a simple carbon balance of the measured CO and CO_2 mass emissions. Stove emissions are captured in a hood after 22 times volumetric dilution. Mass based CO and CO_2 emissions are then measured using a Non-Dispersive Infrared (NDIR) Sensor. For the one step combustion reaction shown in Eq. (14), the parameters d and g are determined from the NDIR measured CO/CO_2 emissions, and the firepower is calculated as shown in Eq. (15) with the previously assumed fuel chemistry and heating value of Chapter 3.

$$aC_X H_Y O_Z + b(O_2 + 3.76N_2) \rightarrow dCO_2 + eH_2O + fO_2 + b(3.76N_2) + gCO$$

$$(14)$$
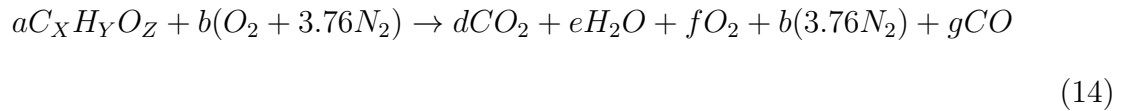
$$\dot{Q}_{in} = \left(a \text{ in } \frac{kgmol}{s} \right) \cdot \left(\text{Heating Value in } \frac{kJ}{kg} \right)$$
$$\cdot \left(\text{Molecular Weight in } \frac{kg}{kgmol} \right) \tag{15}$$

The single step reaction shown in Eq. (14) includes the combustion of gaseous volatiles as well as the surface oxidation of leftover carbon char. The two processes require different amounts of oxygen and have different heat release values. Some error results as the proportion of carbon originating from each process is unknown. However, this effect is minimized as wood volatiles contributions (on a mass basis) are much larger than those from char oxidation. Moreover, after temporal averaging their proportion remains relatively constant. Remaining error is assumed negligible relative to other effects.

4.2 Temperature

Heitor and Moreira [13] provide a good discussion of in-flame temperature and species sampling. Bulk flow temperature is measured using a K-type thermocouple placed at the approximate center of the chimney about 1cm above the chimney exit. The temperature field is likely non-uniform in both the axial and radial directions. An integrated array of thermocouples could be used to address this effect, however at the cost of added complexity and flow intrusion. For this research a single thermocouple is thought to be sufficient. The axial location was determined visually as a trade off between a location after the flame, but before entrainment air. Consistent location is more important the initial location choice, as temperature trends will be examined more closely than absolute values.

4.3 Mass Flow Rate and $\%O_2$

Stack exhaust volumetric $\%O_2$ measurements are used in determining actual stove mass flow rate. Mass flow rate is calculated from stack exhaust $\%O_2$ as shown in Eq. (16)-(18). $\%O_2$ measurements are taken using the O_2 analyzer function of a NO_x 5210 made by ECM (Los Altos, CA). The accuracy of the O_2 analyzer was verified with a 3 point calibration prior to use. The sampling location is the same as the thermocouple and care is taken to sample at a rate no higher than 1% of total stove airflow to avoid affecting stove behavior. The analyzer measures wet $\%O_2$ values, the dry values were arrived at by first passing the sampled airflow through a desiccant.

Stack exhaust $\%O_2$ is related to the single step reaction given in Eq. (14) as shown in Eq. (16). For a dry $\%O_2$ measurement, e is equal to zero. By substituting element conservation equations taken from the reaction in Eq. (14) into Eq. (16), the molar rate of oxygen (b) can be calculated as a function of only the molar rate of fuel (a, calculated using Eq. (15)) and the fuel composition ($C_X H_Y O_Z$) as shown in Eq. (17). Finally, the mass flow rate of air is arrived at by multiplying by the molecular weight as shown in Eq. (18).

$$\%O_2 = \frac{f \cdot 100}{d + e + f + 3.76b} \tag{16}$$

$$b = \frac{a\left(z - 2x - \frac{y}{2}\right)\left(50 - \frac{\%O_2}{2} - \%O_2 \cdot ax\right)}{\%O_2 \cdot 4.76 - 100} \tag{17}$$

$$\dot{m}_A = b \; \frac{kgmol}{s}\left(32 + 3.76 \cdot 28 \frac{kg}{kgmol}\right) \tag{18}$$

4.4 Temporal Syncing of Instrumentation

Sampling with the thermocouple is essentially instantaneous. Time delay for NDIR sampling was determined through spiking to be approximately 70 seconds. The O_2 sensor delay is estimated to be about 45 seconds, determined by comparison of the raw data between the thermocouple, NDIR, and the O_2 sensor.

4.5 Measuring Particulate Matter

Particulate matter data was measured for each 15 minute sample using gravimetric analysis. PM10 data was taken by first using a URG Corporation 2000-30ENB cyclone to remove particles as near above the 10μm cut point as possible (specifications indicate the actual cut point to be 13μm). Downstream of the cyclone, Whatman PTFE (Fisher Scientific $\#05 - 717 - 5$) teflon filters of 47mm diameter and a 2μm pore size were used to collect PM. PM samples were taken after dilution at the top of the fume hood near the NDIR sampling point. Sampling area was about 1/680 of the total flow area. From previous experience with this setup, the limit of detection (LOD) has been calculated to be 15μg, with a limit of quantification for a sample to have statistical significance at 51μg. For this setup, PM measurements were greater than the LOD/LOQ, however some samples, if taken for less than 15 minutes would likely not reach the LOD/LDQ.

5   Validation Results and Discussion (Without Cook Piece)

Experimental data taken from the four validation test runs is compared with model predictions in Figure 8-16. Model behavior is shown for a loss coefficient of 0.5 and for the ideal case with a loss coefficient of one. The two stove geometries are summarized Table 1.

5.1   Temporally Averaged Results

Figure 8 shows the averaged $\%O_2$ values resulting from the firepower sample points taken in each of the four tests with comparison to the model predictions. The corresponding mass flow rate values as calculated from the $\%O_2$ measurements using Eq. (17) and (18) are shown in Figure 9. Error bars indicate one standard deviation in the firepower and $\%O_2$ or mass flow values calculated from the 15 minute data sample. The experimental validation data agrees well with the model predicted behavior.

The validation data shown in Figure 8 and 9 is in agreement with the interesting model prediction of a decreasing mass flow rate with increasing firepower. Higher uncertainty is observed at lower firepowers. These firepowers are harder to create and maintain steadily when burning the stove by hand. These lower firepowers also have decreased mixing and uniformity throughout the chimney.

Corresponding validation temperature data is shown in Figure 10. Trends are predicted well, but in this case the sampled data lies closer to the ideal model predictions. The lower than expected measured temperatures are likely due to chimney wall radiative and convective heat loss. The loss coefficient used in Eq. (8) and (9) only accounts for lowered chimney effect; the temperature is still calculated for the ideal case. A second loss coefficient can be introduced into Eq. (1) accounting for
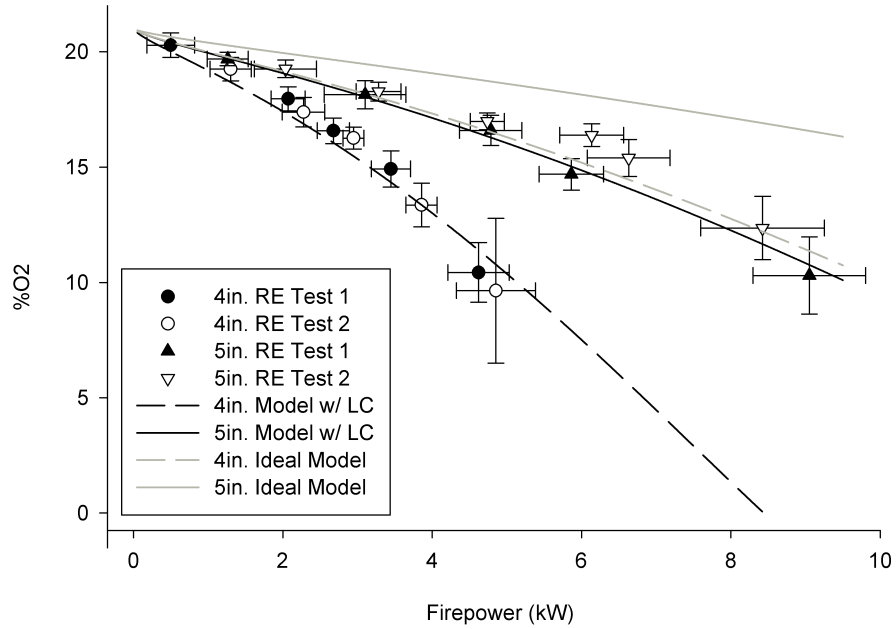
Figure 8: Temporally averaged $\%O_2$ experimental validation results with comparison to model predicted behavior.

lost heat in the heat addition equation. Up to one third of the firepower over a typical stove operation is thought to be lost to the stove walls; if this loss coefficient is set to 0.65-0.75 the model predictions agree well with the validation measurements. However this estimate may be too high for the steady state, and for a relatively efficient fiberfrax insulated rocket elbow. Error may also be caused by the thermocouple location as discussed in Chapter 4.2. Flames were observed to reach past the thermocouple at high firepower, releasing additional heat after thermocouple temperature measurement.

5.2 Instantaneous/Un-averaged Results (Scatter Plots)

The scatter plots shown in Figure 11 and 12 were created using the raw, un-averaged, temperature, $\%O_2$, and the corresponding firepower for each sample. Both geometries are shown with the 4in. diameter plotted in a lighter shade. Model predicted behavior
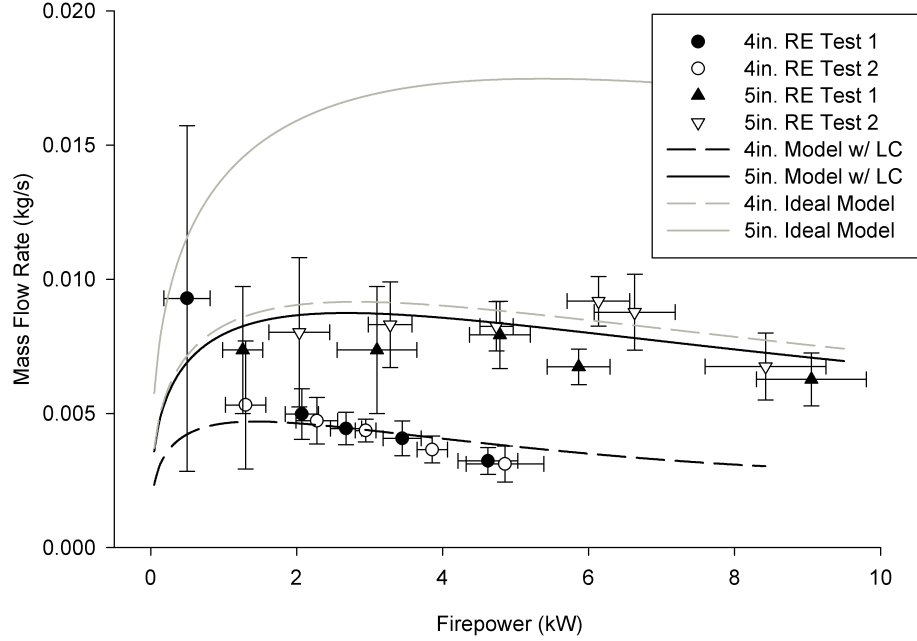
Figure 9: Temporally averaged mass flow rate experimental validation results with comparison to model predicted behavior.

is again shown for comparison as in Chapter 5.1. The plots include data sampled at 0.7hz from all four test runs, including transient periods between 15 minute data samples. The data has been corrected for the time delay between sensors as described in Chapter 4.4. The data fits well considering the inherently transient nature of the stove (evident for example in the raw data shown in Figure 7). These plots provide further assurance that the model physics are applicable and raise the question of whether shorter, or no temporal average could be used.

5.3 Carbon Monoxide Emissions

Although the model does not currently predict stove emissions, some initial data has been sampled. Modified combustion efficiency is a commonly used metric for biomass cooking stove CO emissions, and is defined as shown in equation Eq. (19),
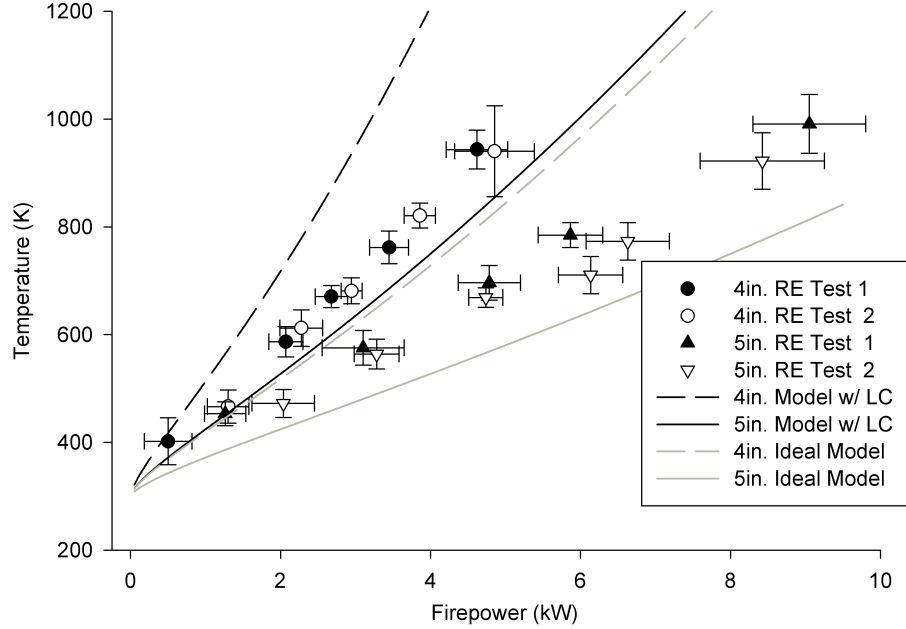
Figure 10: Temporally averaged temperature experimental validation results with comparison to model predicted behavior.

where CO and CO_2 values are in mole/volume fraction. For complete combustion, all CO is oxidized and combustion efficiency is 100%. CO modified combustion efficiency (MCE) temporal averages for the 15 minute samples of Chapter 5.1 are shown in Figure 13 along with model predicted excess air ratio behavior. Measured, temporally averaged, excess air ratio behavior is shown with comparison to model predicted values in Figure 14.

$$\text{MCE} = \frac{CO_2}{CO + CO_2} \tag{19}$$

The initial results suggest that the excess air ratio is a promising tool for reducing carbon monoxide emissions. Higher combustion efficiency is observed at higher firepowers with correspondingly lower excess air ratios. Improved CO oxidation is likely explained by the reduced quenching and increased temperature at these decreased excess air ratios. The modified combustion efficiency trend is consistent between the

26
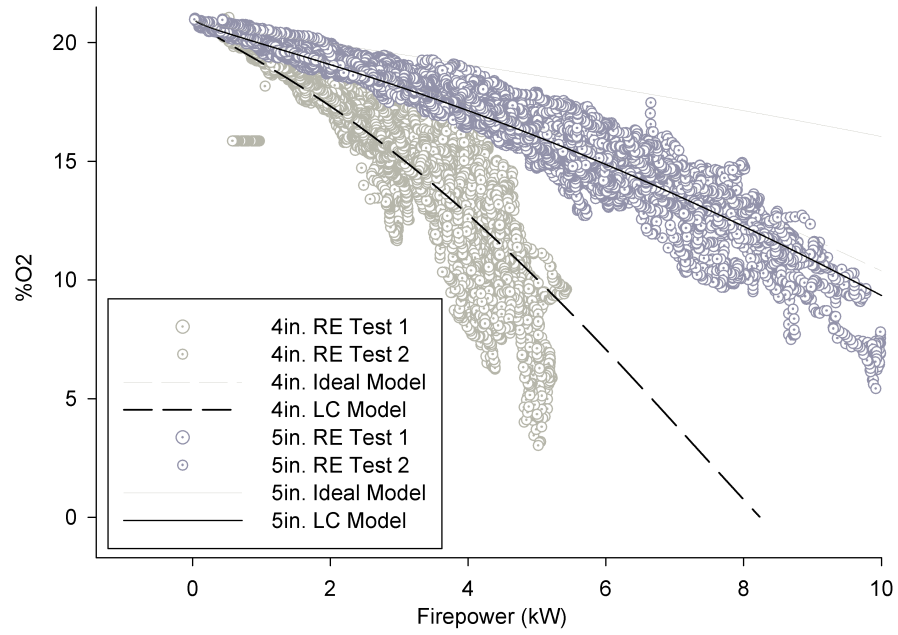
Figure 11: Instantaneous/un-averaged $\%O_2$ validation results with comparison to model predicted behavior.
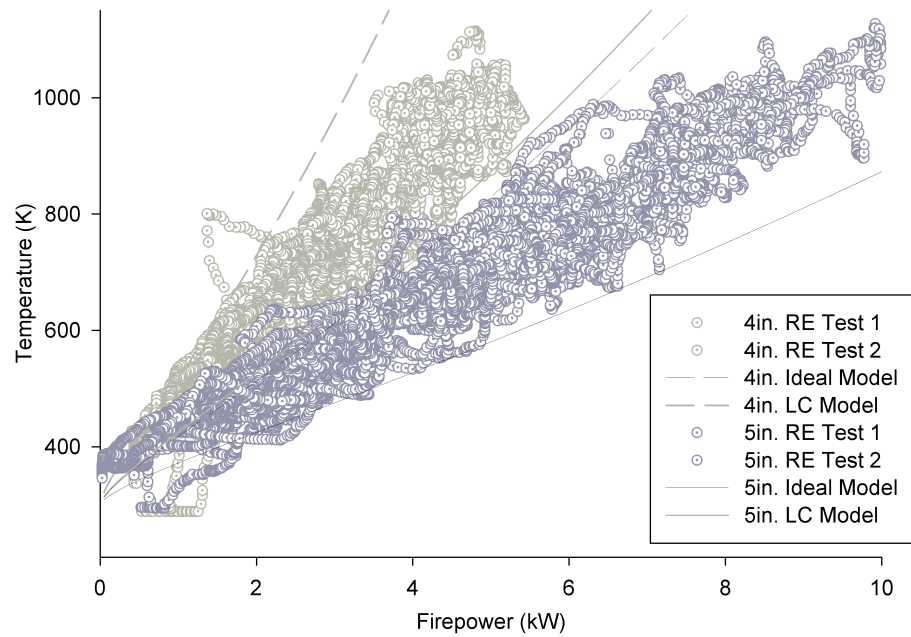
Figure 12: Instantaneous/un-averaged temperature validation results with comparison to model predicted behavior.

27
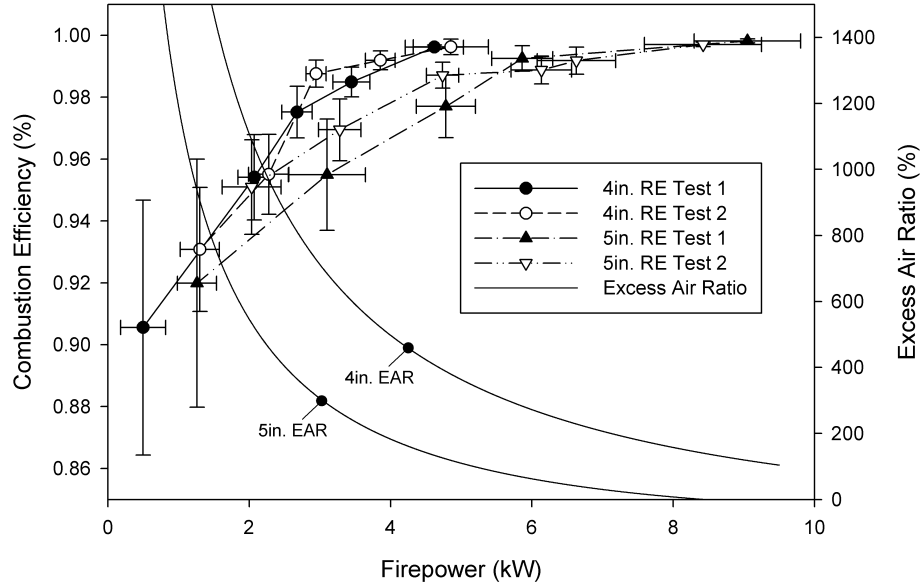
Figure 13: Temporally averaged modified combustion efficiency validation results.

two geometries, but offset to slightly higher firepowers for the larger stove; excess air ratio is correspondingly offset, in agreement with the previous argument. This behavior can be explored further by plotting MCE directly vs. the excess air ratio, as shown in Figure 15.

When plotted with an excess air ratio axis, the modified combustion efficiency of the two rocket elbow geometries are no longer offset from one another; the four curves have been significantly compressed into one trend. The 5in. rocket elbow, test 2 data, although somewhat improved, remains consistently somewhat above the other three curves.

5.4 Stove Firepower Range

The stoves were operated in a typical manner over the range of firepowers which seemed appropriate for cooking use. High firepower data points were determined by the highest practical fueling rate that could be conveniently maintained. The
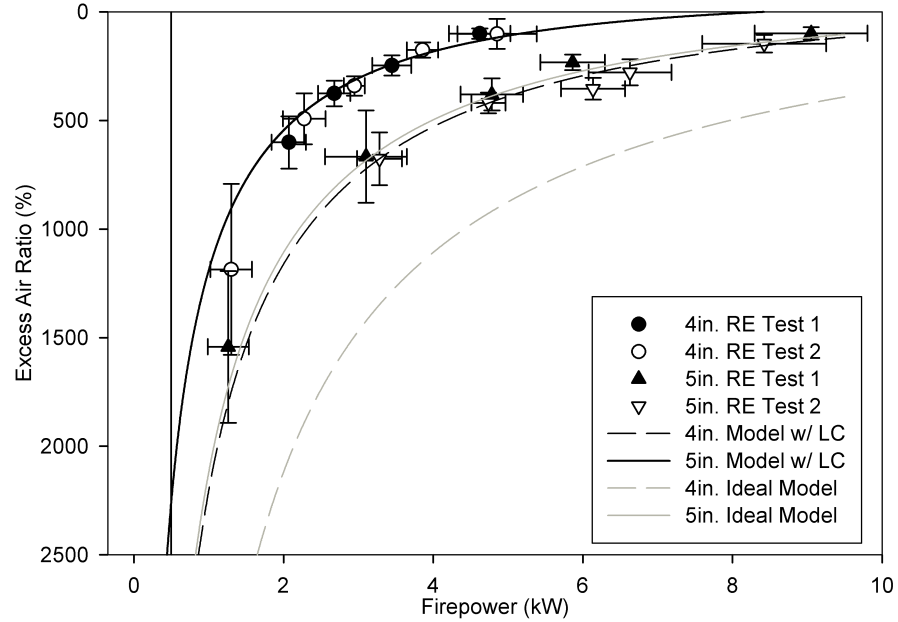
Figure 14: Temporally averaged excess air ratio validation results with comparison to model predicted behavior.

operating range of the 5in. rocket elbow geometry is observed to be higher than that of the 4in. geometry in all of the validation sampling. The larger stove has higher excess air ratios for a given firepower, and it is interesting to note the upper firepower limit occurred at very similar excess air ratios. For ideal fuel/air mixing, the maximum stove firepower was predicted to occur at 0% excess air ratio. In both cases, the maximum firepower was observed at about 100% excess air ratio. Accounting for less than ideal mixing, excess air ratio appears to explain the upper limit of a stove's firepower range. Moving beyond 0% excess air ratio in fueling/pyrolysis rate, one would expect to see no further increase in firepower, but a decrease in combustion efficiency. It appears thus far, that radiative feedback for driving pyrolysis rate has not been a limiting factor.
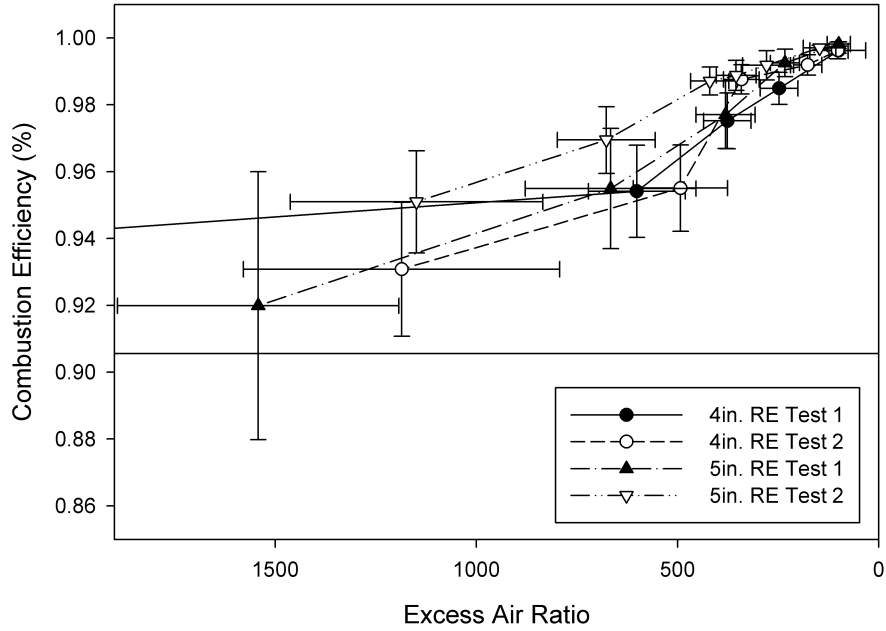
Figure 15: Excess air ratio vs. modified combustion efficiency.

5.5 Particulate Matter Emissions

Particulate matter below approximately $10\mu g$ for the 15 minute validation samples are shown in Figure 16 in the form of an emissions factor (EF). EF is a way of normalizing PM emissions to firepower and is defined using as shown below in Eq. (20).

$$EF = \frac{\text{g of Particulate Matter}}{\text{kg of Fuel Burned}} \qquad (20)$$

The initial data shown in Figure 16 is interesting but more data is needed to make conclusions. All test runs exhibit lowered emissions factors in some medium firepower range; however, this range is not consistent between the four test runs, or within the two runs for each stove size. It is unclear whether the parameters of the model presented herein will be useful in understanding/improving particulate matter emissions.
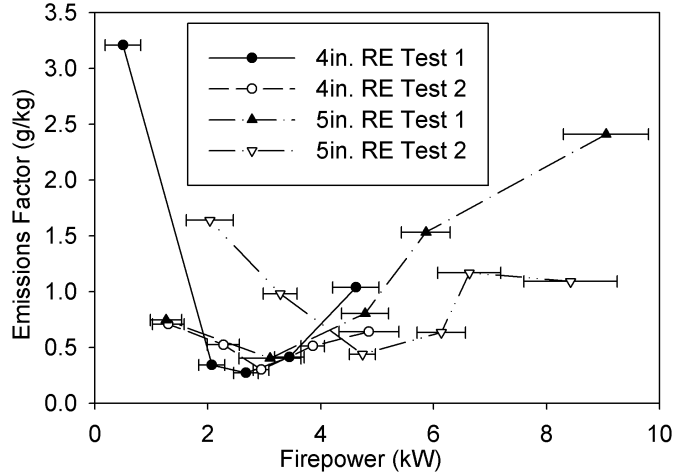
Figure 16: PM10 emissions factor for validation samples.

5.6   High Firepower, Low Excess Air Ratio without Cook Piece

The CO modified combustion efficiency, trends discussed in Chapter 5.3 suggest a lower limit to efficient combustion at low firepower and high excess air ratio. A similar limit may exist at very high firepowers; and for the opposite reason, as combustion approaches an oxygen starved region at high firepowers and low excess air ratios.

Excess air ratio has also been shown to provide some insight into the practical firepower operating range of a stove. At zero percent excess air ratio, or sooner due to poor mixing, an absolute maximum firepower is expected as air supply is exhausted.

5.6.1   Experimental Setup

The fiberfrax insulated 4in. rocket elbow, without a cook piece in place, as used in Chapters 4-5.5 will be used here as well. CO, CO_2, temperature, and $\%O_2$ data is recorded and used as in previous validation, described in Chapter 4. Boht temporally averaged (analogous to Chapter 5.1) and instantaneous scatter (analogous to Chapter 5.2) data will be examined. 15 minute sampling will be attempted for consistency with previous validation results, however it may not be possible to maintain very

high firepowers for this length and shorter averages may be necessary. Two sampling periods will be recorded inside the firepower range of previously recorded validation results to insure consistency and continuity. Firepower will then be increased for two or three sampling periods at higher firepower than previously recorded. An attempt will be made to reach the highest possible firepower for this stove configuration.

5.6.2   Results and Discussion

Attempting to perform the experiment, it has become apparent that an oxygen starved region will not occur in a practically important manner for the rocket elbow stove without a cook piece in place. Although combustion in the stove chimney is limited by the excess air ratio behavior of the stove, combustion will simply proceed after the chimney exit with entrainment air. In this case (and with the current experimental setup) a firepower increase will be recorded, however the combustion heat release after chimney exit has no practical meaning or usefulness to actual cooking operation. It is also interesting to note that for the case of combustion with entrained air after chimney exit, poor CO emissions were not observed (particulate matter data was not taken).

Combustion in the chimney however, is still practically limited by the excess air ratio, and for the stove with a cook piece in place, as examined in Chapter 8, results will be shown to be much more interesting.

6 Loss Coefficient Analysis

The loss coefficient, (C), included in Eq. (7)-(9) and discussed briefly in Chapter 2.3 will now be analyzed more completely. This coefficient is used to account for two main inefficiencies: viscous losses due to stove wall friction and geometric flow disturbances, and a reduction of chimney effect due to the unrealistic point heat addition assumption of Chapter 2.1. For each contribution a loss coefficient will be defined and its magnitude examined using the literature, computational fluid dynamics, and analytical/theoretical methods.

In both cases the reacting (combustion) nature of the flow will be necessarily neglected. This effect likely increases the turbulent energy, thus reducing the proportion of energy lost to viscous effects.

6.1 Viscous Losses and the Restriction Coefficient

Viscous losses including wall friction and geometric flow disturbances induce mixing and flow separation resulting in irrecoverable viscous dissipation of energy. Flow disturbances due to geometry are often termed "minor losses," as they are often small relative to frictional losses in common industry applications. The opposite is true here; frictional losses will be shown to be relatively insignificant and the "minor loss" terminology will be avoided, the term "geometric loss" will be used instead.

Both frictional and geometric losses are commonly included in Bernoulli's Equation as a sum of the lost pressure head ($\sum h_L$), as shown in Eq. (21).

$$\frac{P_1}{\rho g} + \frac{v_1^2}{2g} + z_1 = \frac{P_2}{\rho g} + \frac{v_2^2}{2g} + z_2 + \sum h_L \tag{21}$$

Including this term into the Chapter 2.2 use of Bernoulli's equation, Eq. (5), yields Eq. (22). All terms have also been multiplied by a factor of ρg in order to work with energy terms as opposed to the pressure head terms of Eq. (22).

$$\Delta P_{1-2} = gh(\rho_{Amb} - \rho_H) = \frac{1}{2}\rho_H v_H^2 + g\sum_i \rho_i h_{L,i} \tag{22}$$

The head loss term is commonly calculated using a "resistance coefficient," (K_L), as defined in Eq. (23). This resistance coefficient is essentially the proportion of the flow kinetic energy that will be lost in overcoming viscous losses.

$$h_{L,i} \equiv K_{L,i}\frac{v_i^2}{2g} \tag{23}$$

A resistance coefficient, $K_{L,i}$ is included for each i viscous loss. v_i is the characteristic velocity at loss i. For now we will consider this coefficient to be a table lookup value depending mainly on geometry. The magnitude and more complex dependence of this resistance coefficient will be discussed in Chapter 6.2-6.3.

Substituting Eq. (23) into Eq. (22) gives Eq. (24).

$$gh(\rho_{Amb} - \rho_H) = \frac{1}{2}\rho_H v_H^2 + \frac{1}{2}\sum_i \rho_i K_{L,i} v_i^2 = \Delta P_{1-2} \tag{24}$$

From Eq. (24) it is observed that losses will depend on each $K_{L,i}$ and the kinetic energy at i given by $\rho_i v_i^2$. The kinetic energy at i will vary depending on the velocity and density at each i position in the stove. By conservation of mass, the product of the velocity, cross sectional area, and density will remain constant and equal to the mass flow rate, as shown in Eq. (25). With Eq. (25), for a given total mass air flow rate, if the density at i is known, the kinetic energy at i can be calculated.

$$\rho_i v_i A = constant = \dot{m}_A \tag{25}$$

Density (and with the ideal gas law, temperature), varies in a complex manner with both position and time. In order to reach a practical solution, it will be assumed that each i viscous loss takes place either in the hot or cold flow region of the stove. With this assumption, the summation can be split as shown in Eq. (26).

$$gh(\rho_{Amb} - \rho_H) = \frac{\rho_H v_H^2}{2} + \frac{\rho_H v_H^2}{2} \sum K_{L,H} + \frac{\rho_C v_C^2}{2} \sum K_{L,C} \tag{26}$$

Eq. (25) is used to relate the cold and hot flow velocities as shown in Eq. (27). Substituting for v_C into Eq. (26) yields Eq. (28).

$$v_C = \frac{\rho_H}{\rho_C} v_H \tag{27}$$

$$gh(\rho_{Amb} - \rho_H) = \frac{\rho_H v_H^2}{2} + \frac{\rho_H v_H^2}{2} \sum K_{L,H} + \frac{\rho_H v_H^2}{2} \left(\frac{\rho_H}{\rho_C}\right) \sum K_{L,C} \tag{28}$$

Solving for the mass flow rate as in Chapter 2.2 (this time with the viscous loss terms included) yields Eq. (31), where the loss coefficient would be defined as shown in Eq. (32) by inspection and for consistency with its use in Eq. (7)-(9).

$$gh(\rho_{Amb} - \rho_H) = \frac{\rho_H v_H^2}{2} \left(1 + \sum K_{L,H} + \left(\frac{\rho_H}{\rho_C}\right) \sum K_{L,C}\right) \tag{29}$$

$$gh(\rho_{Amb} - \rho_H) = \frac{\rho_H \left(\frac{\dot{m}_A}{\rho_H A}\right)_H^2}{2} \left(1 + \sum K_{L,H} + \left(\frac{\rho_H}{\rho_C}\right) \sum K_{L,C}\right) \tag{30}$$
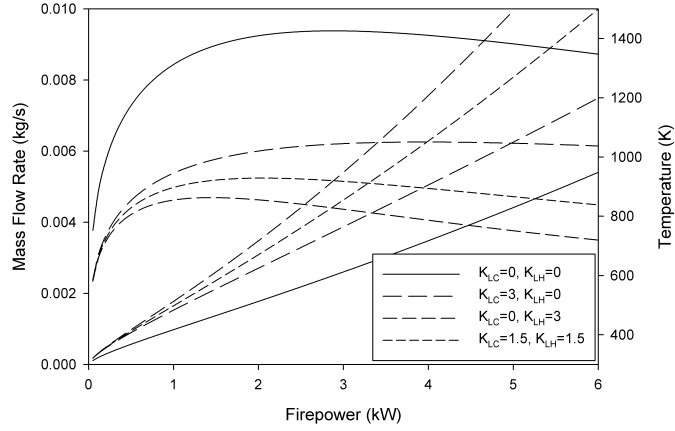
Figure 17: The effect of $K_{L,C}$ and $K_{L,H}$ restriction coefficients

$$\dot{m}_A = \frac{A}{\sqrt{1 + \sum K_{L,H} + \left(\frac{\rho_H}{\rho_C}\right) \sum K_{L,C}}} \left(\frac{P}{R_s T_H}\right) \sqrt{2gh \left(\frac{T_H - T_{Amb}}{T_{Amb}}\right)} \qquad (31)$$

$$C_{\text{Viscous Losses}} \equiv \frac{1}{\sqrt{1 + \sum K_{L,H} + \left(\frac{\rho_H}{\rho_C}\right) \sum K_{L,C}}} \qquad (32)$$

From Eq. (32) it is interesting to note the ρ_C/ρ_H scaling difference between a restriction assumed in the cold flow region compared to the same restriction in the hot flow region. For restrictions applied to the cold flow region, the loss coefficient is no longer independent of the stove flow and operating firepower. If all restrictions are assumed to take place in the hot flow conditions, C remain constant for stove operation as before. With this ρ_C/ρ_H scaling, a fitting will contribute significantly higher losses in the hot flow, especially at higher firepowers. This behavior is summarized in Figure 17, where C is assumed to have a value of 0.5 as in Chapter 5. For $C = 0.5$, using Eq. (32), for consistency the restriction coefficient sum will be equal to three as in Figure 17.

6.2 Restriction Coefficient Values from Theory and Literature

The magnitude and dependence of the restriction coefficient introduced in Chapter 6.1 will now be discussed using analytical/theoretical techniques and published results. For industry applications, turbulent internal flow is of greater interest than the mainly laminar flow encountered here. Consequently, the theory and coefficient inputs for turbulent flow viscous losses are included in most fluid dynamics textbooks; their laminar extensions are less developed and coefficient inputs harder to find.

In either case the results are for fully developed flow. The "entry length" necessary to reach this condition is often estimated by approximately ten times the flow diameter, ($L_{entry,lam.} \approx 10D$). This suggests a length of about 1m, or three times the length of the entire stove flow through the rocket elbow. This inaccuracy should be noted, but is also necessarily neglected.

For application of the restriction coefficient as defined in Chapter 6.1, Eq. (23), to low Reynolds number, laminar flow, the restriction coefficient often takes on a Reynolds number dependence. The restriction coefficient is usually related inversely to the Reynolds number as shown in Eq. (33), where a lower Reynolds number leads to an increased restriction coefficient.

$$K_L = \text{Constant}/Re \tag{33}$$

With this dependence, stove flow Reynolds Number over stove operation must be determined. Stove flow Reynolds number will vary with mass flow rate, as well as the temperature dependence of viscosity, as shown in Eq. (34).

$$Re \equiv \frac{\rho V D}{\mu} = \frac{\dot{m}_A}{\rho A} \frac{\rho \sqrt{A/\pi}}{\mu(T)} = \frac{\dot{m}_A}{\mu(T)\sqrt{A\pi}} \tag{34}$$

37
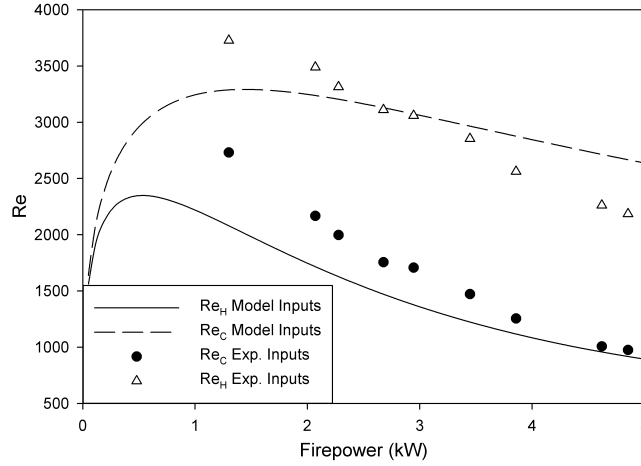
Figure 18: Reynolds number for a 4in. rocket elbow from experimental and model predicted temperature and mass flow rate.

Reynolds number has been calculated from the model predicted behavior of Chapter 3 (for a 0.5 loss coefficient), as well as the experimental data from Chapter 5, the results are shown in Figure 18. The observed inflection point results from the competing effects of temperature and mass flow rate in Eq. (34).

6.2.1 Wall Friction Losses

Wall friction viscous losses are well understood for both turbulent and laminar internal flow; the lost pressure head is often written as shown in Eq. (35), where f is the Darcy friction factor. The resistance coefficient of Chapter 6.1 can then be defined as shown in Eq. (36).

$$h_L = f \frac{L}{D} \frac{v^2}{2g} \tag{35}$$

$$K_L = f \frac{L}{D} \tag{36}$$

38

For internal flow, transition from laminar to turbulent flow is often considered to take place at $Re \approx 2,300$. From Figure 18, stove flow is observed to be in the laminar to transitional region. In the laminar region, the friction factor f is conveniently independent of wall roughness, and depends only on the Reynolds number as shown in Eq. (37). This equation is common to virtually all fluid dynamics textbooks and is again intended for fully developed flow.

$$f = \frac{64}{Re} \tag{37}$$

The resulting restriction coefficient is shown in Figure 19 with comparison to other geometric viscous losses to be determined in Chapter 6.2.2. Frictional losses are observed to be much less significant than geometric viscous losses and can likely be considered negligible.

6.2.2 Geometric Losses

Geometric losses for a rocket elbow without a cook piece in place will be calculated here as the sum of a 90° elbow, an inlet (infinite sudden contraction) and an exit (infinite sudden expansion). For the case of a stove with the cook piece in place, the rather unique cook piece and drip pan impingement/channel flow restriction would not be easily determined, and is not considered here.

Edwards et al. [10] provides a readily applicable, experimentally determined, relationship for the 90° elbow geometry. As discussed, the laminar relationship takes the form of Eq. (33), and is given below in Eq. (38). A transition to turbulent flow was reported at $Re \approx 900$, after which a constant $K_{L,elbow}$ value of 0.9 was observed. From Figure 18, this transition may be within the expected Reynolds number range of the stove. This behavior is shown with comparison to other losses in Figure 19.
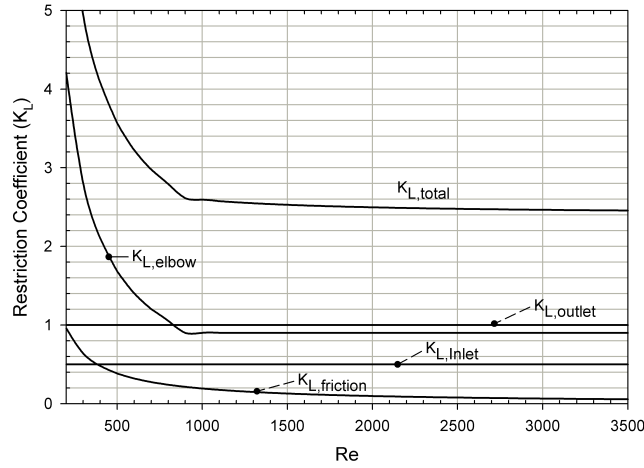
Figure 19: K_L contributions and total from theory and literature.

$$K_{L,elbow} = 842/Re \qquad (38)$$

Readily applicable Restriction coefficient values for the sudden infinite contraction and expansion were not found. It is hypothesized that a sudden expansion of a large diameter ratio will approach the behavior of the infinite expansion/contraction at an inlet or exit. Edwards et al. [10] provides data for sudden expansion/contraction for diameter ratios up to two and one half respectively. The results show a transition to turbulent behavior at a Reynolds number of 200. Oliveira et al. [20] reports the same transition for diameter ratios up to four. From the predicted Reynolds number behavior of Figure 18, flow will likely remain turbulent for this geometry. For turbulent flow, (constant) restriction coefficients are commonly available, and a value of $K_{L,inlet} = 0.5$ and $K_{L,outlet} = 1$ for the inlet and outlet respectively have been taken from Cengel and Cimbala [6].

6.2.3   Total

Chapter 6.2.1 and 6.2.2 viscous losses are summarized in Figure 19 for the Reynolds number range shown in Figure 18. The various viscous losses are shown together for

comparison. Wall friction losses are observed to be relatively negligible. Reynolds number dependence and higher restriction coefficients are observed at low Reynolds number.

6.3 Computational Fluid Dynamics

Wall friction and geometric restriction coefficient values are also calculated using computational fluid dynamics (CFD) for comparison to the results of Chapter 6.2. Results will again be for the 4in. rocket elbow geometry without a cook piece in place. The Fluent® 6.3 Solver is used; default setting should be assumed if not otherwise noted. The restriction coefficient can be calculated from the pressure difference and mass flow rate as follows.

Starting with Eq. (24), a constant density will be used (either hot or cold), and solving for $K_{L,i}$ yields Eq. (40).

$$\Delta P_{1-2} = \frac{1}{2}\rho v_2^2 \left(1 + K_L\right) \tag{39}$$

$$K_{L,i} = 2\rho\Delta P \left(\frac{A}{\dot{m}_A}\right)^2 - 1 \tag{40}$$

A mass air flow rate will be forced through rocket elbow geometry, the resulting pressure drop will then be measured from the numerical CFD solution, and a restriction coefficient is calculated using Eq. (40). The equation calculates the difference between the CFD measured pressure drop and the ideal Bernoulli's Equation predicted pressure drop for the given mass flow rate.

6.3.1 Model Setup

A fluid volume has been created for the 4in. rocket elbow geometry with a sudden inlet and exit into ambient reservoirs. A mass flow inlet is prescribed at the inlet reservoir boundaries and is used to set and vary the mass air flow rate through the rocket elbow geometry. The outlet reservoir is prescribed as a pressure outlet. Inlet and outlet adjacent faces as well as the rocket elbow chamber walls are prescribed as wall boundary conditions.

The pressure difference used in Eq. (40) is measured by subtracting the integrated total pressure at the mass flow inlet from that of the pressure outlet. The model is run to standard Fluent® residual based convergence criteria. The integrated total pressure at inlet and outlet is also monitored while iterating for an additional and practical measure of convergence.

As discussed in Chapter 6.2, laminar to transitional flow is expected during stove operation. Laminar governing equations are likely sufficient for simulation, however a Spalart-Allmaras turbulence model, as described in Chatterjee and Deviprasath [7], will also be used for comparison. Spalart-Allmaras is a one-equation turbulence model, and likely the simplest option. It is well suited for low Reynolds Number flow and relatively course boundary layer meshing as described in the Fluent® users manual.

The resistance coefficient should be dependent on geometry and Reynolds number only as described in Chapter 6.2. This expectation will be verified for a varying fluid temperature, as will be important to stove flow. The energy equation is unnecessary and is not included in the governing fluid dynamics of the CFD model; temperature enters only through its effect on density and viscosity. Results will be compared for three fluid property temperatures over the typical stove operating range: 300K, 800K, and 1100K.
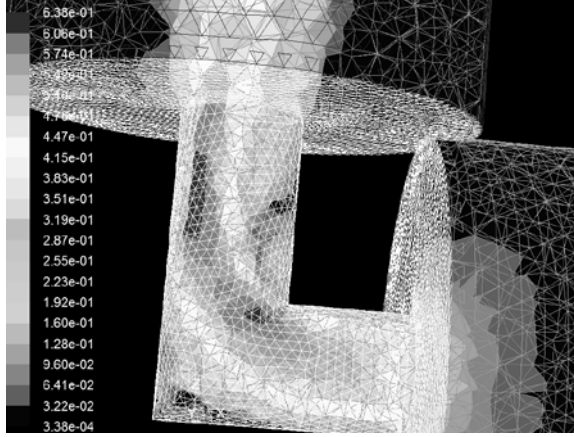
Figure 20: CFD mesh with velocity contour results

A 3D tetrahedral element mesh will be created, and will be refined at wall boundaries. Bulk element and boundary layer mesh sensitivity are performed and will be described in Chapter 6.3.2. The resulting fluid volume, mesh, and a velocity contour solution is shown in Figure 20.

6.3.2 Mesh Sensitivity

Mesh sensitivity studies are performed in order to insure mesh independence of the CFD numerical solution. "Bulk" tetrahedral mesh element size is varied first. Integrated total pressure difference results, for use in Eq. (40), are shown in Table 2 for each element size and for the laminar and Spalart-Allmaras turbulence model. The mesh element count is also included to note increasing computational cost. Results are observed to be remarkably unaffected for all studied mesh sizes and models.

Element Size	# of Elements	ΔP Result (N/m^2)	
		Laminar	Spalart-Allmaras
24mm	31,320	0.0396	0.0408
21mm	41,648	0.0393	0.0406
18mm	60,414	0.0397	0.0409
15mm	98,059	0.0396	0.0411
12mm	144,804	0.0401	0.0417

Table 2: Bulk mesh sensitivity

An 18mm "Bulk" mesh size is chosen. Although any of these meshes appear sufficient thus far, the 18mm element will likely provide a balance between computational cost, geometric resolution and a transition to the boundary layer mesh. Boundary layer mesh sensitivity is studied next. Fluent's® boundary layer adapt tool is utilized to mark and refine the first two elements bordering all wall boundaries. The results are shown in table Table 3. A 2nd and 3rd boundary layer adaption is also included, made in a similar manner to the first, but using only the first cell at wall boundaries.

18mm Bulk Mesh w/...	# of Elements	ΔP Result (N/m^2)	
		Laminar	Spalart-Allmaras
No BL Adaption	60,414	0.0397	0.0409
1st BL Adaption	94,735	0.0423	0.0439
2nd BL Adaption	163,895	0.0456	0.0472
3rd BL Adaption	526,369	0.0418	0.0434

Table 3: Boundary layer (BL) mesh sensitivity.

After the 2nd adaption, some inconsistent results are observed. This is likely caused by a transition from the near wall profile modeling to direct calculation. Observed wall Y+ values for these meshes support this theory. The results after this region are again consistent. Considering the purpose and desired accuracy of this study, and for reduced computational cost, the 1st BL adaption mesh will be used.

6.3.3   Model Results

Computational fluid dynamics model results are shown in Figure 21 for the Reynolds number range expected from Figure 18.

The three model temperatures have varying density and viscosity properties. The varying density is apparent in the three temperature curves when plotting vs. mass flow rate. However, when plotting with Reynolds number, the three temperatures produce only one curve, and the Reynolds number dependence/temperature independence of the resistance coefficient is observed.
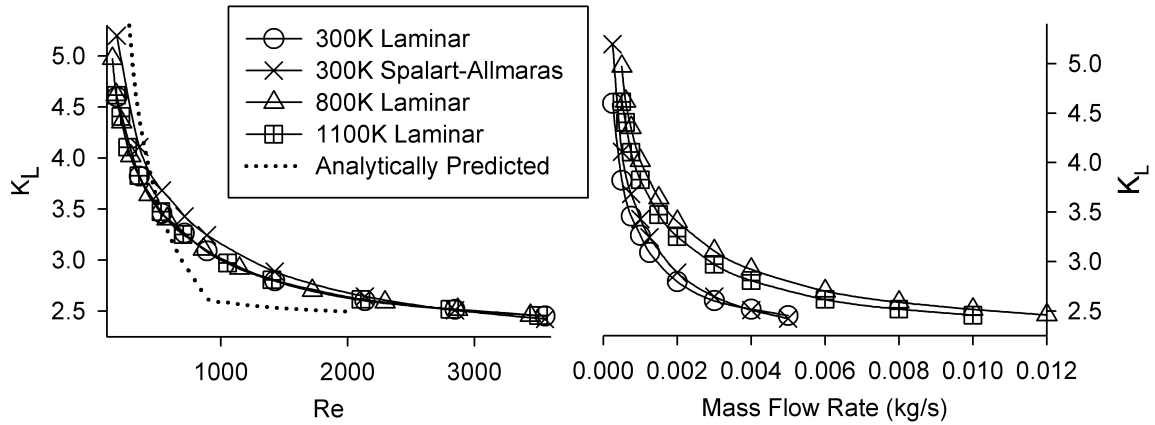
Figure 21: CFD predicted K_L plotted vs. Re and mass flow rate

Although the Spallart-Allmaras turbulence model showed consistency with the laminar physics in the sensitivity studies, one curve has been produced with the turbulence model to check for trend consistency. The resulting values are negligibly higher and the same trend is produced.

The total restriction coefficient predicted in Chapter 6.2 and shown in Figure 19 is also included for comparison. The two results are relatively close considering their independence, the complexity of the flow, and the noted inaccuracies of Chapter 6.2.

6.4   Distributed Heat Addition

In Chapter 2.1, the assumption was made that heat addition takes place entirely at the base of the chimney. In reality combustion heat addition is distributed throughout the chimney at the flame, as well as at the solid fuel surface reactions. Heat addition at the base of the chimney produces a maximum chimney effect; the reduction of available chimney effect resulting from heat released after this point will be estimated.

Uniform heat addition over the chimney height, as defined in Eq. (41), is proposed as an improved assumption over the point heat addition of Chapter 2.1. This uniform

heat addition profile can be used to illustrate the mechanism by which chimney effect is reduced, as well as estimate its magnitude.

$$\frac{d\dot{Q}_{in}}{dz} \equiv \frac{\dot{Q}_{in,Total}}{h} \tag{41}$$

The non-premixed flame and its heat release are inherently complex and transient. A more realistic profile than that of Eq. (41) could not be determined, and a brief argument is made for the assumed profile. The combustion rate at the flame is principly limited by the diffusion of reactants to the flame reaction zone. For constant chemistry, and a relatively consistent flame environment throughout the chimney, this diffusion rate and the resulting heat release at the flame will remain relatively constant. If the flame is considered to be approximately the height of the chimney, and narrowing effects are ignored, a relatively uniform distribution of heat release is suggested.

The proposed uniform heat release profile is illustrated in Figure 22a, with comparison to the initially assumed point addition.

(a) Heat addition   (b) Temperature   (c) Density
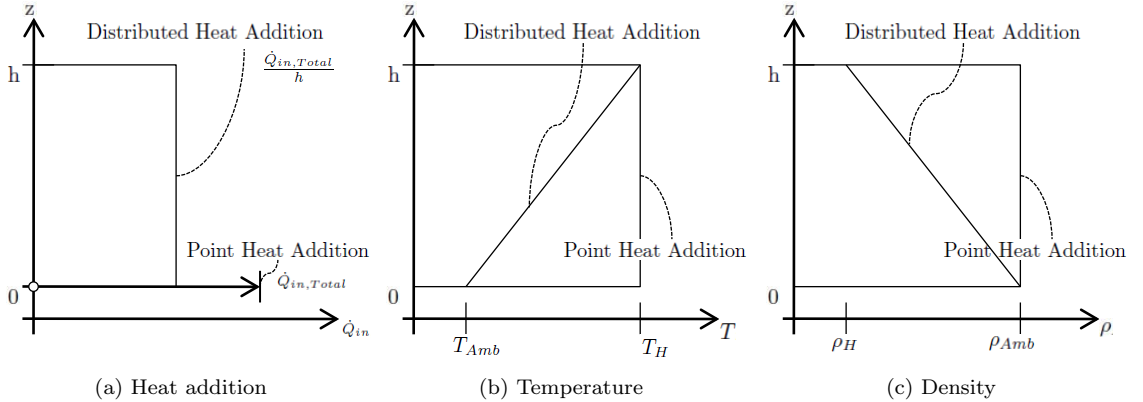
Figure 22: Heat addition, temperature, and density profiles for point and distributed heat addition.

Assuming an adiabatic system and constant specific heat, the differential form of Eq. (1), as shown in Eq. (42), will be used to calculate the chimney temperature profile.

$$dQ_{in} = \dot{m}_A c_p dT \qquad (42)$$

Multiplying both sides of Eq. (42) by a differential chimney height section and rearranging yields Eq. (43).

$$d\dot{Q}_{in}dz = \dot{m}_A c_p dTdz$$

$$\frac{d\dot{Q}_{in}}{dz}dz = \dot{m}_A c_p dT \qquad (43)$$

Substituting the heat release profile defined in Eq. (41), rearranging and integrating as shown yields Eq. (44).

$$\frac{\dot{Q}_{in,Total}}{h}dz = \dot{m}_A c_p dT$$

$$\frac{\dot{Q}_{in,Total}}{h}\int_0^z dz = \dot{m}_A c_p \int_{T_C}^{T(z)} dT$$

$$\frac{\dot{Q}_{in,Total}}{h}z - 0 = \dot{m}_A c_p \left(T(z) - T_C \right) \qquad (44)$$

Solving Eq. (44) for $T(z)$, a linear relationship with chimney height is observed as shown in Eq. (45). The temperature profile is also shown in Figure 22b with comparison to the point heat addition case.

$$T(z) = \left(\frac{\dot{Q}_{in,Total}}{h\dot{m}_A c_p} \right) z + T_C \qquad (45)$$

With Eq. (45), and at the bottom of the chimney, $z = 0$, the temperature is calculated to be $T(0) = T_C$. At the top of the chimney for $z = h$, the equation simplifies to the form of Eq. (1) for the point heat addition case. The final T_H at the chimney exit ($z = h$), is observed to be the same as the in the point addition case.

With the temperature profile shown in Figure 22b, heat conduction along the flow is now possible and will be considered briefly using the Peclet Number, (Pe). Pe is defined as shown below in Eq. (46) as the ratio of bulk flow to conduction heat transfer.

$$\text{Pe} \equiv \frac{\rho L V c_p}{k} = \frac{LV}{\alpha} = \frac{\text{Bulk heat transfer}}{\text{Conduction heat transfer}} \tag{46}$$

Where L and V are the characteristic length and velocity, and α is the thermal diffusivity ($\alpha_{air} \approx 2.2160 \times 10^{-5} m^2/s$ @ 300K, 1atm). Using a 0.21m chimney height for the characteristic length, and typical stove velocities from 2-4m/s, Pe will be over 18,000, and heat conduction can be safely neglected.

With the temperature profile shown in Figure 22b, and once again using the ideal gas law, the resulting density profile takes the shape shown in Figure 22c. The point heat addition density profile is also shown for comparison. This density profile has the effect of reducing the chimney effect driving pressure difference of Eq. (3), repeated below in Eq. (47). The integral, $\int_3^2 \rho(h)dh$, can be performed geometrically by inspection of the density profile shown in Figure 22c. The integral can be observed at this point to be of half the magnitude of the point heat addition profile. This integral result is shown below in Eq. (48). For any given density profile, the resulting pressure drop can be visualized in this manner.

$$\Delta P_{1-2} = g\rho_{Amb}h - g\int_3^2 \rho(h)dh \tag{47}$$

$$\Delta P_{1-2} = g\rho_{Amb}h - g\left[\frac{1}{2}\left(\rho_{Amb} + \rho_H\right)h\right] \tag{48}$$

Further simplifying Eq. (48) as shown in Eq. (49), leads to half of the pressure drop when compared to Eq. (4), as previously observed from Figure 22c.

$$\Delta P_{1-2} = \frac{1}{2}gh\left(\rho_{Amb} - \rho_H\right) \tag{49}$$

Using this pressure drop to calculate the chimney effect in the same manner as Chapter 2.2, Eq. (5)-(9), this halved pressure drop is shown to translate to a mass and volume flow rate $1/\sqrt{2}$ times lower than before, as shown in Eq. (51). This leads to a loss coefficient as defined in Eq. (52)

$$\frac{1}{2}gh\left(\rho_{Amb} - \rho_H\right) = \frac{1}{2}\rho_H\left(\frac{\dot{m}_A}{A\rho H}\right)^2 \tag{50}$$

$$\dot{m}_A = \frac{1}{\sqrt{2}}\left(\frac{AP}{R_sT_H}\right)\sqrt{2gh\left(\frac{T_H - T_{Amb}}{T_{Amb}}\right)} \tag{51}$$

$$C_{\text{Heat Addition}} \equiv 1/\sqrt{2} \approx 0.707 \tag{52}$$

6.5 Loss Coefficient Summary

The various restriction coefficient models resulting from the Chapters 6.1-6.4 discussion have been introduced into the Chapter 2 stove flow model. The constant loss coefficient has been replaced with the product of the loss coefficient contributions defined by Eq. (52) and (32), as shown below in Eq. (53).

$$\dot{m}_A = \left(C_{\text{Heat Addition}}\right)\left(C_{\text{Viscous Losses}}\right)\left(\frac{AP}{R_s T_H}\right)\sqrt{2gh\left(\frac{T_H - T_{Amb}}{T_{Amb}}\right)}$$

$$= \frac{1}{\sqrt{2\left(1 + \sum K_{L,H} + \left(\frac{\rho_H}{\rho_C}\right)\sum K_{L,C}\right)}}\left(\frac{AP}{R_s T_H}\right)\sqrt{2gh\left(\frac{T_H - T_{Amb}}{T_{Amb}}\right)}$$

$$(53)$$

The loss coefficient is now dependent on the stove flow operating conditions. The equation can be slightly simplified relating the density ratio to a temperature ratio, $(\rho_H/\rho_C = T_C/T_H)$. This equation is solved iteratively as in Chapter 2.4, only the loss coefficient is now updated at each iteration with Eq. (53) to the current stove operating conditions. Resulting loss coefficient behavior over the stove operating range is shown in Figure 23 for four cases:

The first two cases use the theoretical results of Chapter 6.2. The viscous losses due to the 90° elbow geometry can be reasonably applied to either the hot or cold flow region; both cases have been solved and are included in Figure 23. In either case, the Reynolds number is calculated from hot or cold flow properties respectively.

For the third and forth case, a power law curve fit has been applied to the computational fluid dynamics results of Figure 21. The total restriction coefficient, (including viscous and geometric contributions) as a function of Reynolds number is determined and is shown below in Eq. (54). The power law fit results in a coefficient of determination, R^2, value of 97.8%. The resulting $K_{L,total}\left(Re\right)$ has been applied to both a cold, and hot region restriction coefficient ($K_{L,C}$ and $K_{L,H}$) in Figure 23.

$$K_{L,total} = 14.304 Re^{-0.221} \qquad (54)$$
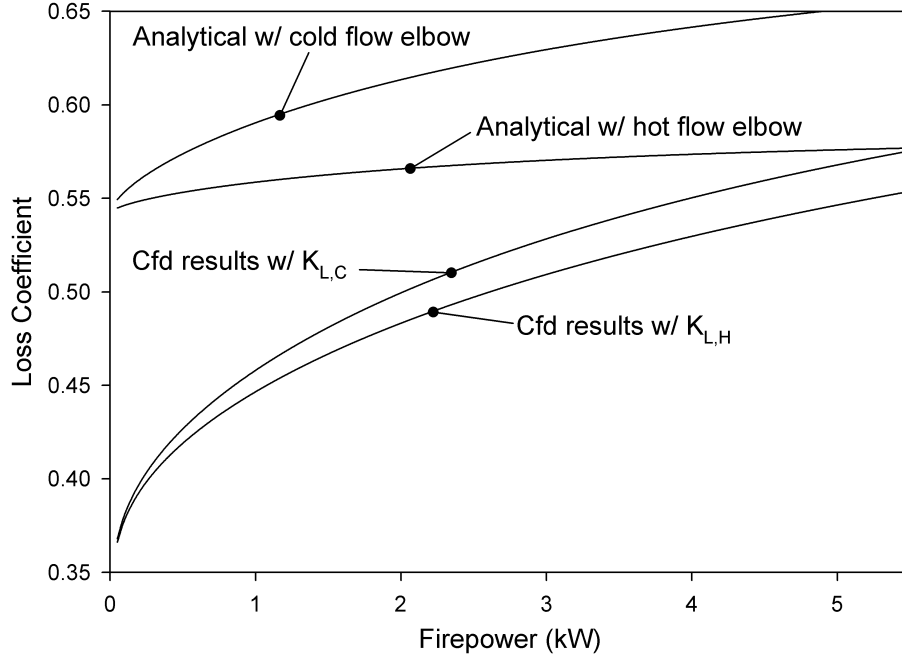
Figure 23: Comparison of loss coefficients for a typical stove operation range.

The accepted inaccuracy associated with assuming a constant loss coefficient is clearly illustrated. The four curves exhibit roughly the same trend. Slightly higher losses are observed at higher firepowers, where an increase in Reynolds number as observed in Figure 18 is competing with a reduction in the $K_{L,C}$ by ρ_H/ρ_C scaling. Considering the noted inaccuracies of Chapter 6.2, the computational fluid dynamics curves are likely of higher accuracy. Further CFD studies would be interesting to investigate the effect of a cook piece, and other common and important geometry possibilities.

Considering the four curves together, the initially assumed and experimentally determined constant value of C=0.5 is shown to be relatively reasonable. Using the computational fluid dynamics results to determine a cold region resistance coefficient, the $\%O_2$ and temperature behavior shown in Figure 24 is predicted. The previously used constant C=0.5 model prediction are shown in a lighter shade for comparison. Experimental data for the 4in. rocket elbow from Chapter 3 is included as well.
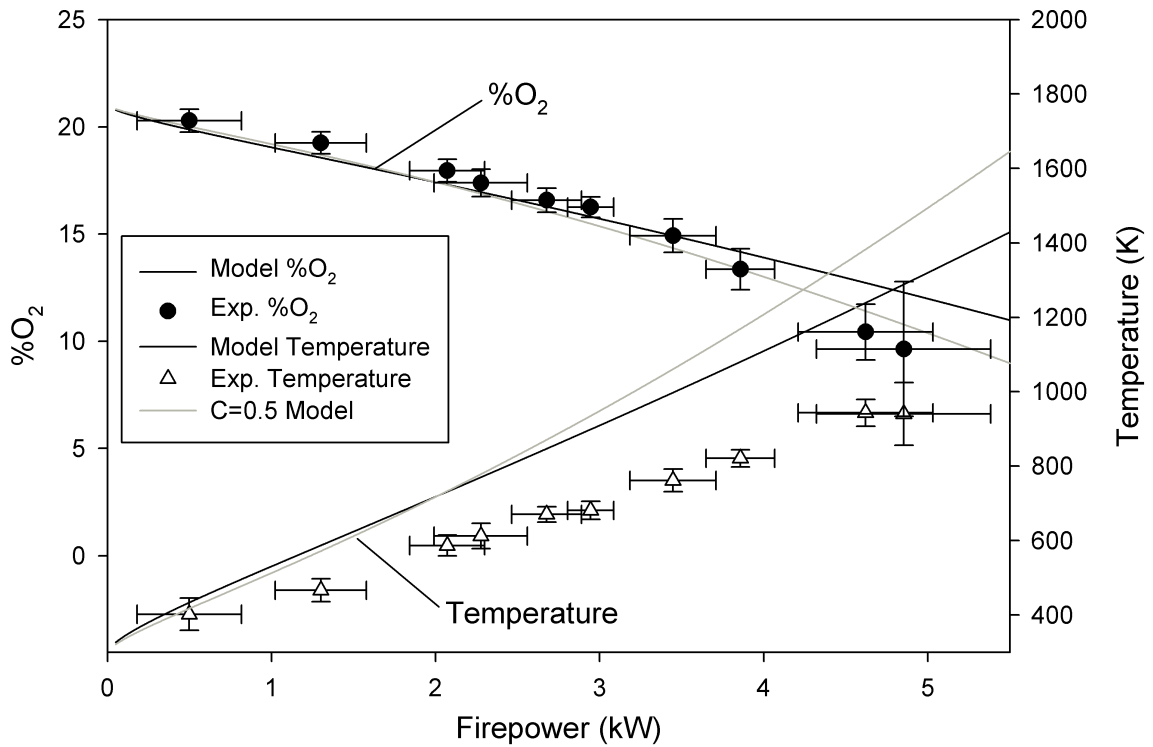
Figure 24: CFD based loss coefficient predicted stove behavior with comparison to without cook piece validation results.

The predicted model behavior is relatively similar. A slightly improved temperature curve (reduced temperatures over prediction) is observed, along with a negligibly worse prediction of $\%O_2$. Considering other necessarily accepted inaccuracies elsewhere, the constant C=0.5 value is probably sufficient and practical.

7 Dimensionless Form

The system of equations derived in Chapter 2 model setup can be further developed into a dimensionless form. Advantages of working in this dimensionless form include scale similarity and reducing the number of independent parameters for experimentation.

In the case of the model presented here, the dimensionless form offers an additional advantage. Solving the dimensionless system of equations to be developed, dimensionless stove behavior is plotted and is independent of stove geometry. The resulting plots can be used as a reference to lookup and calculate solutions without solving the system of equations (in this case iteratively).

7.1 Dimensionless Model Setup

The heat addition and chimney effect equations (Eq. (1) and (9)) defining the simplified stove model developed in Chapter 2, and shown in Figure 3, are repeated below in Eq. (55) and Eq. (56).

$$\dot{m}_A = CA \left(\frac{P}{R}\right) \left(\frac{1}{T_H}\right) \sqrt{2gh \left(\frac{T_H - T_{Amb}}{T_{Amb}}\right)} \tag{55}$$

$$\dot{Q}_{in} = \dot{m}_A c_p \left(T_H - T_{Amb}\right) \tag{56}$$

7.1.1 Dimensionless Chimney Effect Equation

The dimensionless temperature group shown in Eq. (57) can be formed immediately by inspection. This group is likely familiar and is commonly used in many fields.

$$T^* \equiv \frac{T_H - T_{Amb}}{T_{Amb}} \tag{57}$$

Substituting Eq. (57) into Eq. (55) and rearranging yields Eq. (58).

$$
\begin{aligned}
\dot{m}_A &= CA \left(\frac{P}{R} \right) \left(\frac{1}{T_{Amb} \left(T^* + 1 \right)} \right) \sqrt{2ghT^*} \\
&= CA \left(\frac{P}{RT_{Amb}} \right) \left(\frac{\sqrt{2ghT^*}}{T^* + 1} \right)
\end{aligned}
\tag{58}
$$

(P/RT_{Amb}) is the ambient density, (ρ_{Amb}). Substituting ρ_{Amb} and rearranging as shown in Eq. (59), the dimensionless mass flow rate group can be defined as shown in Eq. (60).

$$\frac{\dot{m}_A}{CA\rho_{Amb}\sqrt{gh}} = \frac{\sqrt{2T^*}}{T^* + 1} \tag{59}$$

$$\dot{m}_A^* \equiv \frac{\dot{m}_A}{CA\rho_{Amb}\sqrt{gh}} \tag{60}$$

Using the dimensionless mass flow rate $\dot{m}_A^*$, the final form of the dimensionless chimney effect equation becomes that of Eq. (61).

$$\dot{m}_A^* = \frac{\sqrt{2T^*}}{T^* + 1} \tag{61}$$

7.1.2 Dimensionless Heat Addition Equation

The remaining dimensional equation for heat addition is now considered. For the dimensionless model it becomes convenient to use a mass burn rate of fuel instead of the firepower (resulting from the mass burn rate) used previously, where the two are related as shown in Eq. (62).

$$\dot{Q}_{in} = \dot{m}_F HV \tag{62}$$

Substituting Eq. (62) and Eq. (57) into Eq. (56) and rearranging into Eq. (63), a dimensionless heating value group, (HV^*), is formed as defined in Eq. (64).

$$\dot{m}_F \left(\frac{HV}{c_p T_{Amb}} \right) = \dot{m}_A T^* \tag{63}$$

$$HV^* \equiv \frac{HV}{c_p T_{Amb}} \tag{64}$$

Substituting the dimensionless mass air flow rate defined in Eq. (60), into Eq. (63), yields Eq. (65). A dimensionless fuel mass flow rate, of a similar form to the dimensionless air flow rate of Eq. (60), can be defined as shown in Eq. (66).

$$\dot{m}_F HV^* = \dot{m}_A^* C A \rho_{Amb} \sqrt{gh} T^* \tag{65}$$

$$\dot{m}_F^* \equiv \frac{\dot{m}_F}{C A \rho_{Amb} \sqrt{gh}} \tag{66}$$

Using the dimensionless mass fuel flow rate $\dot{m}_F^*$, the final form of the dimensionless heat addition equation becomes that of Eq. (67).

$$\dot{m_F}^* HV^* = \dot{m}_A^* T^* \tag{67}$$

7.1.3 Air/Fuel Ratio from the Dimensionless Model

The Air/fuel ratio can be conveniently recognized by rearranging Eq. (63) as shown in Eq. (68). HV^* will remain constant for stove operation, and a simple inverse linear relationship between T^* and the AFR is observed.

$$AFR \equiv \frac{\dot{m}_A}{\dot{m}_F} = \frac{HV^*}{T^*} \tag{68}$$

7.2 Dimensionless System Results

Eq. (61) and (65) together define the dimensionless simplified stove flow model analogous to the dimensional case of Chapter 2.4. Stove geometry no longer appears directly in either equation, and enters only through the definition of the dimensionless air and fuel mass flow rates. As in Chapter 3.3 for the dimensional model, geometry parameters appear only together as the product of $CA\sqrt{h}$. This $CA\sqrt{h}$ product essentially scales the dimensional mass air flow rate and firepower to scale similarity (the dimensionless form) for use in Eq. (61) and (65).

Eq. (61) and (65) can be solved iteratively in the same manner as the dimensional system in Chapter 2.4. The simplified (relative to the dimensional model) MATLAB® script is given in Appendix D. The resulting dimensionless stove behavior plot is shown in Figure 25.
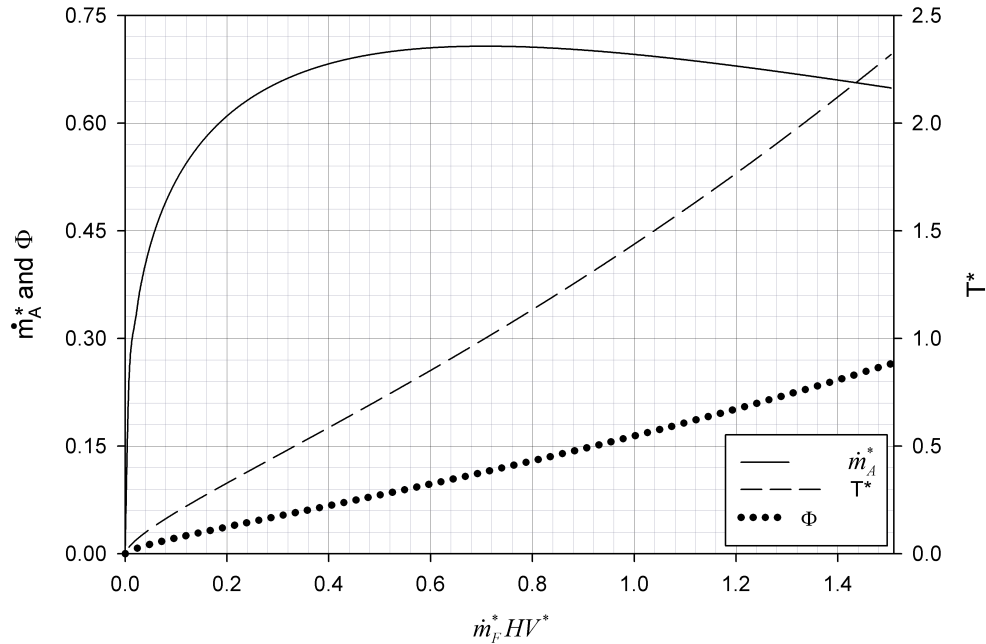
Figure 25: Non-dimensional stove behavior/lookup plot

The x-axis product, $\dot{m}_F^* HV^*$, is analogous to the firepower axis in Figures 4-16. $\dot{m}_F^*$ and T^* are of course analogous to the dimensional $\dot{m}_F$ and T_H, and behave in a similar manner, only scaled.

The dimensionless solution does not require a solution (in this case iterative) for each geometry and firepower of interest. Because the solution shown in Figure 25 is independent of stove geometry, it can be used to lookup solutions for a given stove geometry and firepower of interest without solving the model system. The firepower is first converted to a dimensionless form using Eq. (65) and (64) and the geometry of interest. Figure 25 can then be used to lookup the corresponding dimensionless mass air flow and temperature. These values are then returned to their dimensional form using Eq. (57) and (60) for practical use. For a desired AFR, the corresponding T^* can be easily calculated from Eq. (68), and the corresponding dimensionless air and fuel mass flow rate can be determined from Figure 25 in a similar manner.
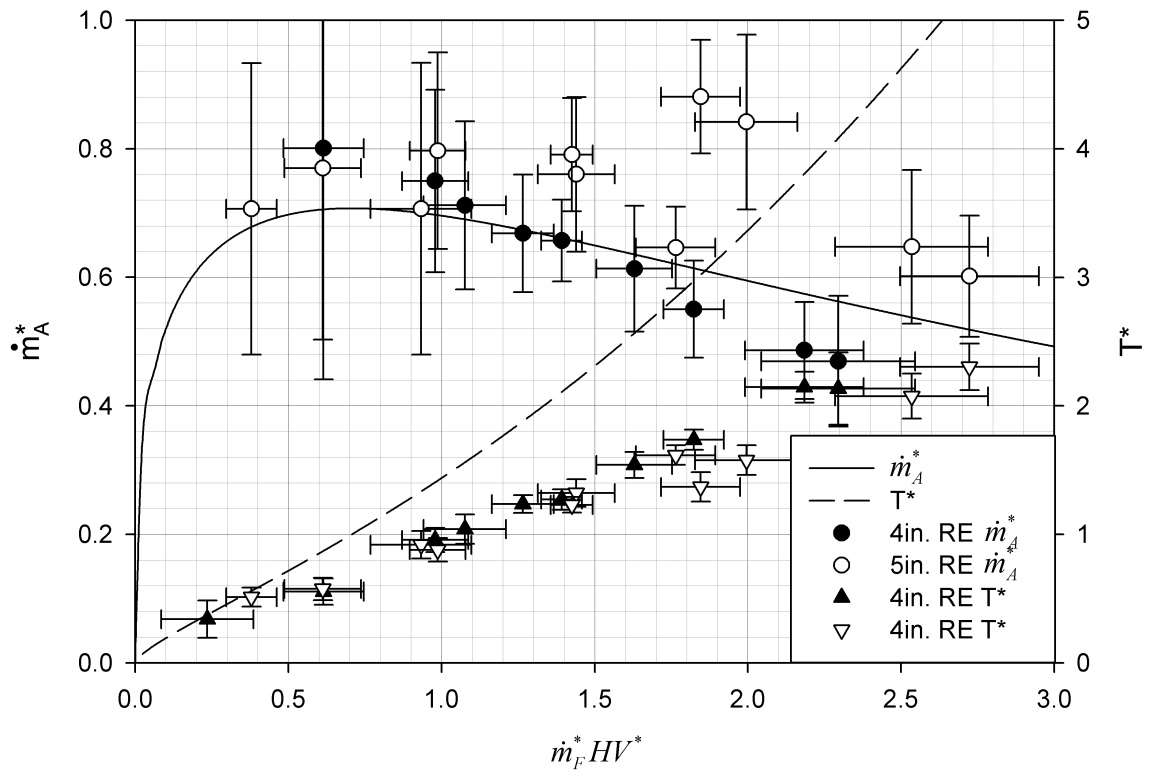
Figure 26: Non-dimensional stove behavior with comparison to validation results.

7.3   Dimensionless Validation Results

In the dimensionless form, experimental data from varying stove geometry can be plotted together on a single plot. Plots analogous to Figure 6 do not exist as the stove behavior is independent of stove geometry. Validation data from Chapter 5 has been plotted in dimensionless form for both validation geometries in Figure 26 with the dimensionless system predicted stove behavior from Chapter 7.2.

The validation data fits well and now follows a single trend line for both stove geometries. Once again measured temperature falls significantly bellow predicted values, likely for the reasons already discussed with dimensional results of Chapter 5.1.

8   With Cook Piece Validation

Chapters 4-5 validation has thus far been for the idealized case of a stove operating without a cook piece in place. This setup has been useful for isolating the basic model physics and assessing model accuracy while minimizing the effect of the unknown loss coefficient and neglected heat transfer. However a stove without a cook piece in place is inherently not useful for actual cooking use. Validation with the cook piece in place will now be discussed to examine model application to practical operation while cooking.

Higher and more significant viscous losses are expected with the cook piece in place due to the more restrictive stagnation and channel flow. The relatively cold, close proximity, and high thermal mass cook piece (including water) will also increase heat loss from the stove flow. These effects are expected, some idea of their magnitude is to be determined. The effect of having the cook piece in place on stove emissions is even less predictable. Emissions data will be recorded as with the previous validation data for examination and comparison.

8.1   Experimental Validation Setup

Setup is similar to the without cook piece validation of Chapters 4 and 5; the fiberfrax insulated 4in. rocket elbow stove is used once again and the previously recorded without cook piece data of Chapters 4 will be used for comparison. The stove has been fitted with an Envirofit model G3300 drip pan as shown in Figure 27. The G3300 drip pan has built in supports for locating the cook piece resulting in an 18mm pot gap at the narrowest point. A stainless steel cook piece of 225mm diameter containing five liters of boiling water is used. The cook piece water temperature will affect the heat transfer rate (with a higher ΔT producing higher rates), therefore the

water temperature must remain consistent between tests. Boiling water is simple to maintain and monitor. The cook piece water is raised to boiling temperature before data sampling.

Two test sweeps will be performed with the cook piece in place; each test sweep consisting of five 15minute data sampling periods as described in Chapters 4. An attempt will be made to hit the firepower points of the previous 4in. rocket elbow validation data of Chapter 5.
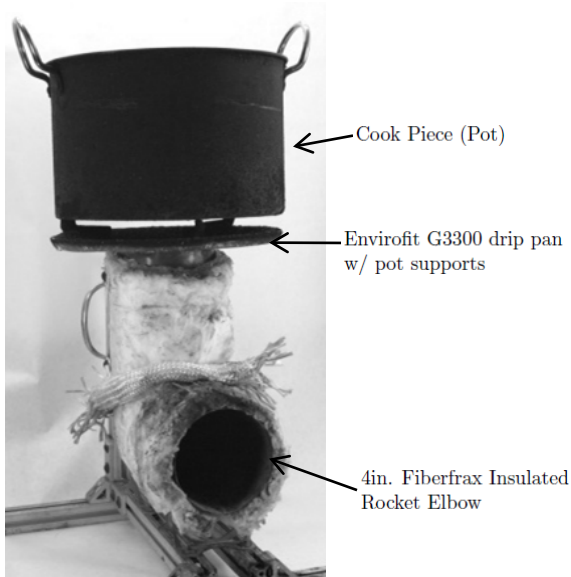
Figure 27: With cook piece validation setup.

CO, CO_2, temperature, and $\%O_2$ data is recorded and used as before, described in Chapters 4. However due to interference with the cook piece, $\%O_2$ sampling and thermocouple location must be located slightly lower than before, in the gap between the drip pan and the cook piece. This location is approximately in the middle of the cook piece drip pan gap and about 10mm lower than without the cook piece in place.

8.2 Validation Results

8.2.1 Bulk Flow Rate and Temperature

With cook piece validation results from the temporally averaged 15 minute data samples of $\%O_2$, mass air flow rate, and temperature are shown in Figure 28-30.

Figure 28: With cook piece $\%O_2$ validation results with comparison to model predicted behavior and without cook piece validation results.

Corresponding without cook piece 4in. rocket elbow validation data from Chapter 4-5 is also shown for comparison in a lighter shade.

Model predicted trends remain in agreement, but at consistently lower flow rates and higher temperatures. This behavior can be explained by the expected increase in viscous losses. A third model predicted curve has been added for an even higher loss coefficient (LC) than those of Chapter 5, where LC=0.35. Predicted behavior with this loss coefficient is in good agreement with the experimental results. This additional loss is higher than initially expected, and burning the stove at firepowers corresponding to the without cook piece validation, as intended, is found to be impossible for some higher powers. The highest firepower that could be achieved in either test run was around 4kW. This will be discussed further in Chapter 9

Two high firepower outliers are observed in the with cook piece validation data. As discussed in Chapter 5.4, exhaust $\%O_2$ and bulk excess air ratio can relate an
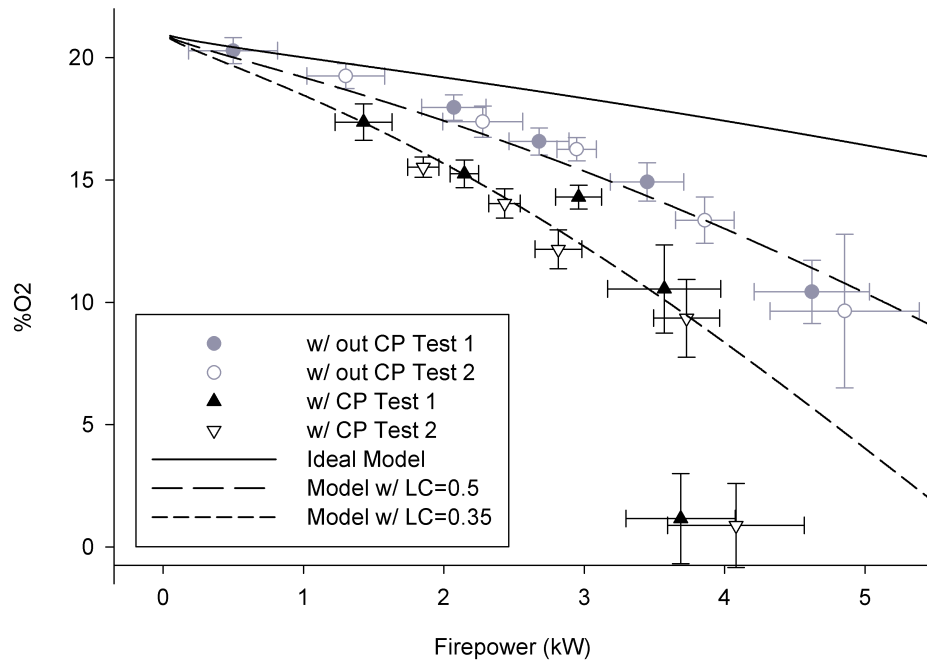
Figure 29: With cook piece mass flow rate validation results with comparison to model predicted behavior and without cook piece validation results.

operating firepower to a stove configuration's firepower range. At this high firepower and for the 0.35 loss coefficient model predicted excess air ratio is around 40%. Measured $\%O_2$ is around 2%. These values are much lower than those reached in the previous validation data for all the but the failed high firepower attempts of Chapter 5.6, and suggest a very high firepower relative to the current stove configuration. Considering the poor mixing inherent to biomass cook stoves of this type, combustion in this region is likely oxygen starved. In this case, unburned volatiles would continue to decreased $\%O_2$, but without the increase in firepower that would have resulted from their combustion. This behavior is in agreement with that of the observed high firepower outliers.

With cook piece validation temperature results in Figure 29 are observed to be higher than that of the 4in. rocket elbow without a cook piece in Chapter 5. Decreased mass air flow with the cook piece in place creates a reduction in thermal mass to be
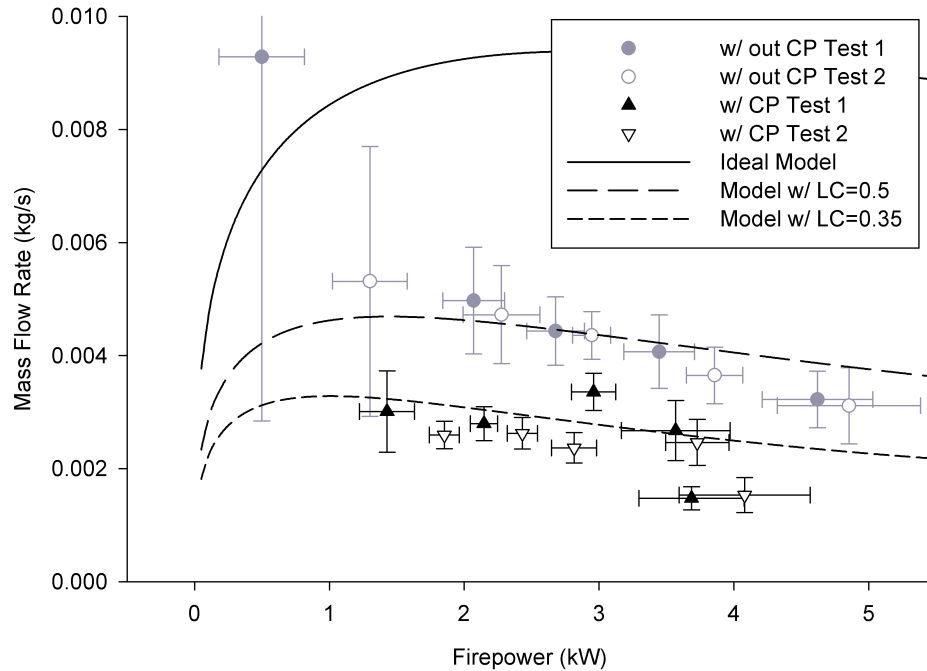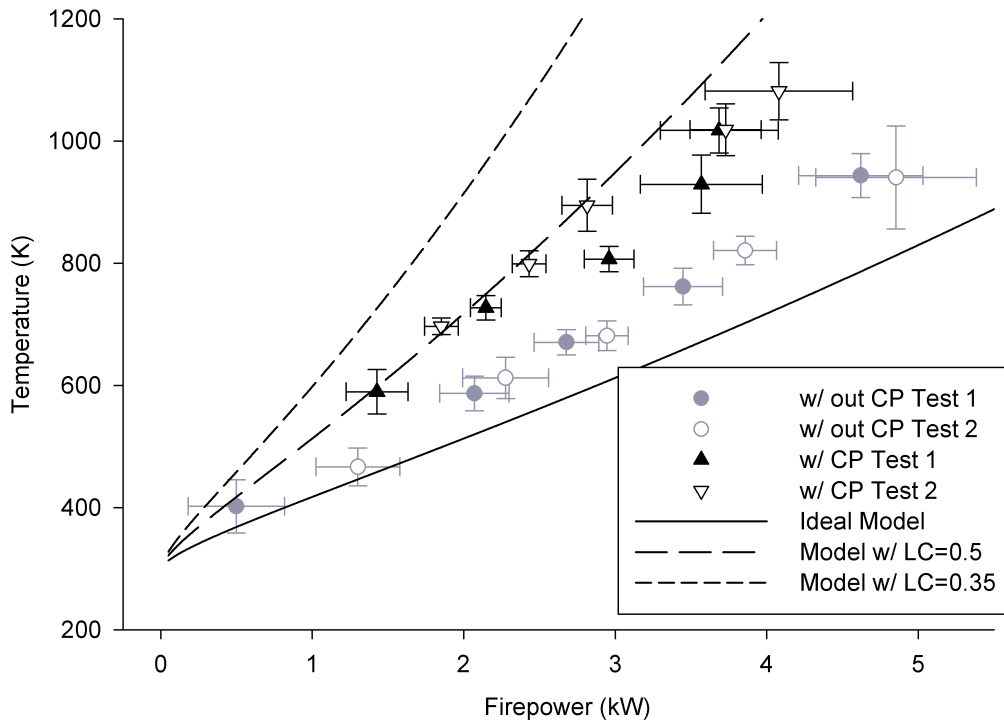
Figure 30: With cook piece temperature validation results with comparison to model predicted behavior and without cook piece validation results.

heated by a given firepower, and thus higher temperatures. This effect is competing with the expected increase in air flow heat loss to the cook piece. With the observed temperature increase, the decrease in thermal mass is observed to be more significant than the increase in flow heat loss. The 0.35 loss coefficient agrees well with the measured $\%O_2$ and mass flow rate, but measured flow temperatures are lower than predicted. This result is consistent with that of the Chapter 5 without cook piece data and is again likely explained by inaccuracies of the adiabatic assumption.

8.2.2   Carbon Monoxide Emissions

With cook piece validation temporally averaged results for CO modified combustion efficiency are shown in Figure 31. The previously discussed high firepower outliers behave in a particularly interesting manner. With these points a sharp reduction in

combustion efficiency is observed. This high power reduction is much steeper than the onset of good combustion with increasing power at lower firepowers.
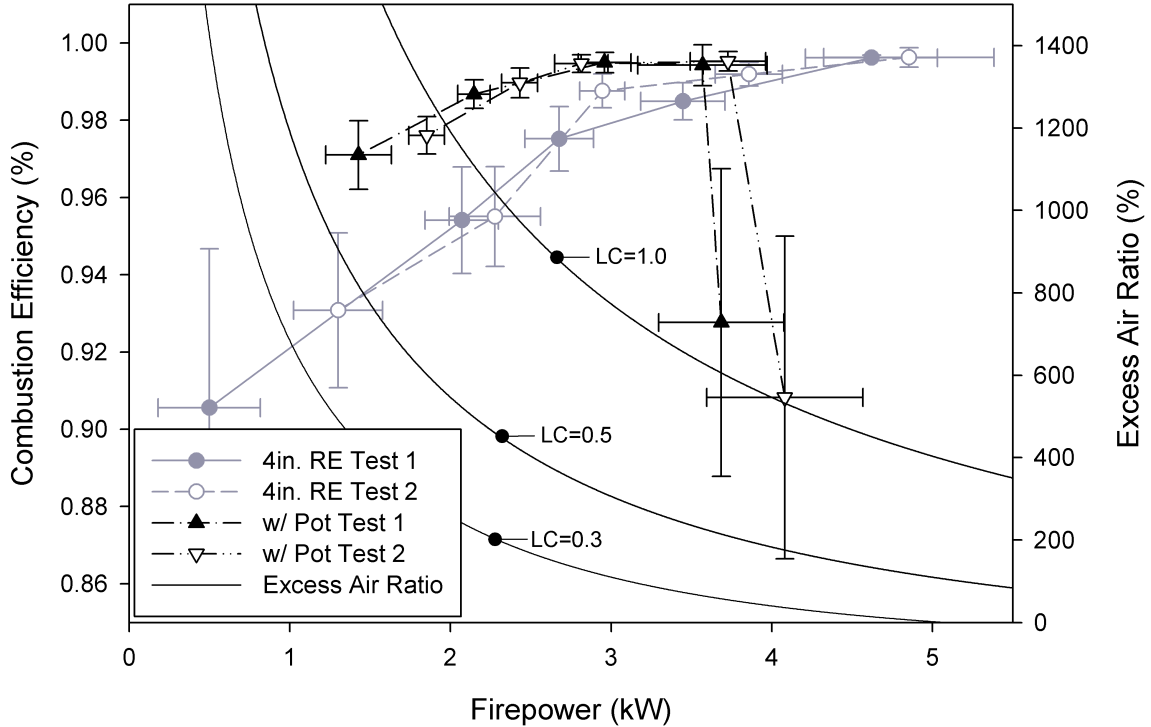
Figure 31: With cook piece CO modified combustion efficiency results with comparison to without cook piece validation results.

In Chapter 5.6 a failed attempt to find a poor combustion limit in this high firepower region is discussed. Chapter 5.6 suggests that as the chimney region becomes oxidizer starved, combustion is able to proceed with entrainment air after the chimney with no significant detriment to CO modified combustion efficiency. It appears that this is no longer the case with the cook piece in place. The exact mechanism or combination thereof responsible for this behavior is uncertain. The following observations may be of significance: entrainment air can no longer be reached immediately at the top of the chimney flow. The flame aerodynamic disturbance of the cook piece may be important. It is also possible that the pot removes enough heat from the flow that combustion can no longer proceeds in an efficient manner after leaving the

chimney and reaching entrainment air.

8.2.3 Particulate Matter Emmissions

Particulate matter emissions are affected in a similar manner as CO. With cook piece PM emissions factor validation results are shown in Figure 32.
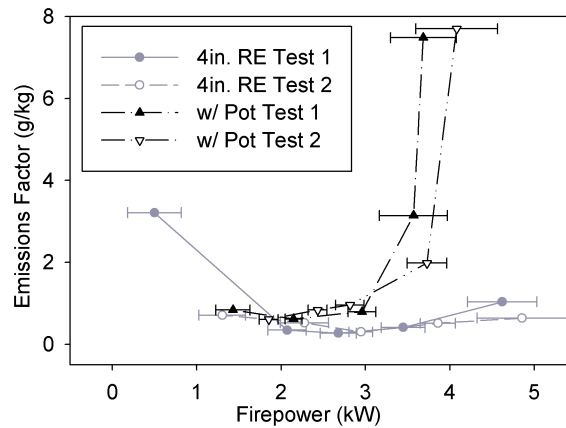
Figure 32: With cook piece PM emissions factor results with comparison to without cook piece results.

The effect of having the cook piece in place on particulate matter emissions was difficult to predict beforehand; two major competing effects are thought to exist. Buildup of particulate matter on the cook piece due to impaction is known to occur, thus removing particulate matter before reaching the filter for gravimetric analysis. Radiative quenching of particles (after formation, but before passing through the flame sheet) is often thought to affect the likelihood of a particle's of oxidation. The relatively cool and immediate cook piece will likely encourage radiative heat exchange from particulate matter, reducing the likelyhood of oxidation.

A steep increase in particulate matter emissions is observed at higher firepowers. No increase was observed at low firepowers as with the without cook piece validation results. As already discussed, the with cook piece stove is likely operating at a much

higher firepower relative to its firepower range. Accounting for this possibility, with cook piece data would be shifted to the right relative to the without cook piece results, and the two curves may be in agreement. This will be discussed further in Chapter 9. For the with cook piece results, low enough firepower sampling may not have been taken to observe the low firepower emissions factor increase. The same may be true for the without pot results at high firepower, although the steep particulate matter increase may also only occur with a cook piece in place as observed with CO modified combustion efficiency.

9 Dimensionless Summary of Emissions Data and an Efficient Combustion Region

Using the dimensionless form developed in Chapter 7, the three stove configurations (4in. and 5in. rocket elbow without cook piece, and 4in. rocket elbow with cook piece) can be plotted concurrently and in sync. Chapter 5 without cook piece and Chapter 8 with cook piece emissions results are shown in Figure 33 plotted with the dimensionless firepower axis, $\dot{m}_F^* HV^*$. The plot shows both carbon monoxide (in the form of modified combustion efficiency) and particulate matter emissions (in the form of an emissions factor).
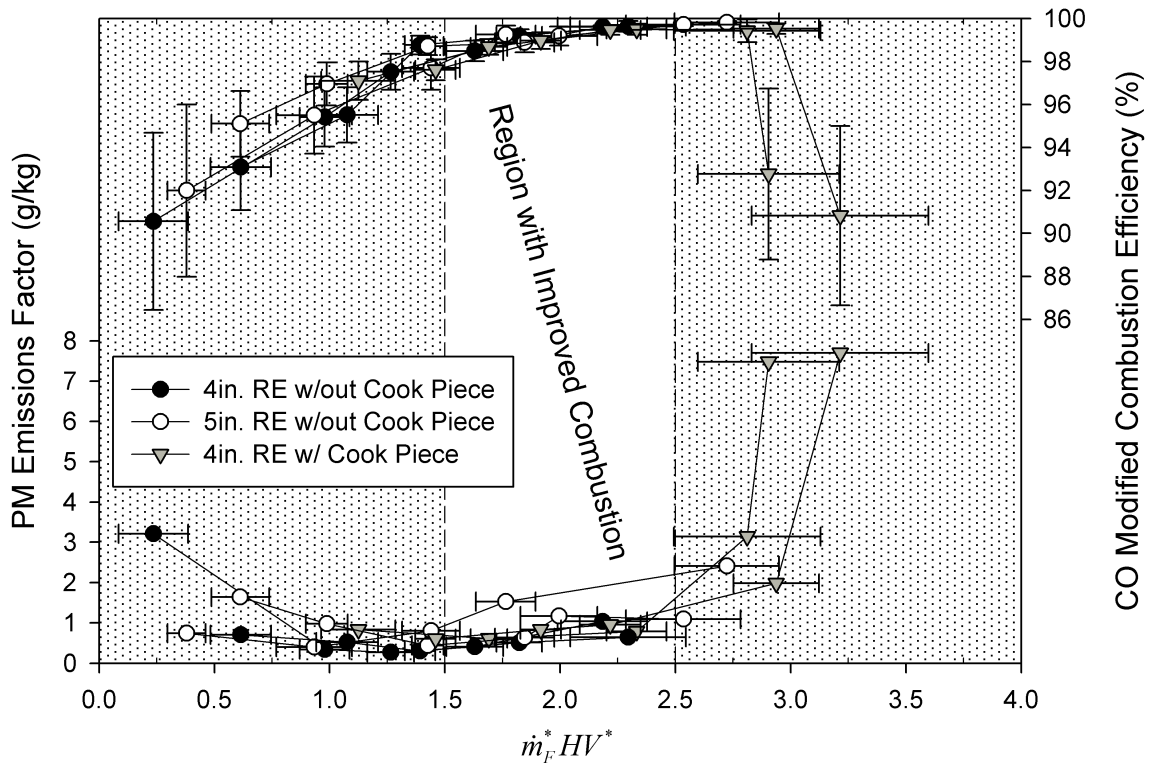
Figure 33: Dimensionless summary of CO MCE and PM EF with improved combustion efficiency region.

Using the dimensionless firepower, the with and without cook piece results contribute to a single trend for both particulate matter and carbon monoxide emissions,

despite the data looking considerably different in the dimensional form of Figures 28-32. In this form both carbon monoxide and particulate matter emissions trends are observed.

Most importantly, an efficient combustion region is suggested in Figure 33 at dimensionless firepowers between 1.5 and 2.5, this region has been marked. Both carbon monoxide and particulate matter emissions are significantly improved in this region, and become deteriorate quickly outside of this region. It is interesting to note from these initial results that the two emissions seem to trend together. For a desired firepower a stove geometry can be calculated to match this efficient combustion region.

10   Conclusion

The simple stove flow model developed herein has shown itself to be both accurate and practically useful in predicting bulk flow rate, temperature, and excess air ratio for a natural convection driven biomass cooking stove from geometry and firepower inputs.

Validation without a cook piece in place has assessed baseline model accuracy, while further validation with a cook piece has explored practical model applications. The primary difference observed between the two configurations was a decrease in the loss coefficient (corresponding to an increase in stove losses) from about 0.5 to 0.35. The with cook piece configuration also allowed the observation of a high firepower limit to efficient combustion.

Although measured temperature trends were very consistent with those predicted by the model, temperature values were consistently over predicted with measured values 20-30% lower than those predicted. A more realistic but also complex loss coefficient was shown to help but not alleviate this problem. Other contributing sources of error have been discussed in Chapter 5.

10.1   Carbon Monoxide Emissions

Although initial results suggest that the bulk excess are ratio may be a useful tool in understanding and effecting biomass cook stove CO emissions, future work is necessary explore this link in the current as well as other stove/fuel configurations. The mechanism by which bulk excess air ratio directly affects CO oxidation throughout the stove at the non-premixed diffusion flame front is not well understood and would certainly be of interest as well.

10.2   The Dimensionless Form

The basic flow physics determined up to this point allowed for the identification of dimensionless stove parameters and the development of a dimensionless form of the stove flow model. This dimensionless form has shown potential as a useful tool for experimentation, especially with emissions results. The dimensionless form was used to consolidate and summarize carbon monoxide and particulate matter emissions results, and an improved emissions region has been suggested.

10.3   Particulate Matter Emissions

Particulate matter emissions data is relatively time consuming and labor intensive to collect, and more data is desired in order to make strong conclusions. However, some initial trends have been observed. Particulate matter has been observed to trend fairly well with CO. This relationship is both interesting and convenient, allowing for reduced emissions to be achieved simultaneously for both emissions criteria. Much like CO emissions trends, the direct mechanisms involved in the observed trends are unknown. Theoretical understanding of particulate matter formation and destruction is likely an even more elusive emissions phenomena then that of CO. Many complex and competing factors such as particle radiative heat transfer, competition for OH radicals, flame length and thickness are thought to be important. Frenklach [11],Roper [22] and Kent and Wagner [17] have been especially thought provoking.

10.4   Thermal Efficiency and Heat Transfer

Although not discussed herein, thermal efficiency and heat transfer model extensions are very likely and have both great potential and important applications. It is unknown what tradeoffs may exist between the observed improved emissions region and

that of improved thermal efficiency. Bulk temperature and mass flow rate model outputs are important inputs for heat transfer studies, perhaps using computational fluid dynamics. Viskanta [32] provides a good review of impingement heat transfer (similar to the stove pot interface) for cases with and without combustion; a theoretical description and several solutions and correlations are presented. However relatively little work has been performed at sufficiently low Reynolds number and nozzle to plate distances for ready application to biomass cooking stoves. In any case (CFD or correlation), the inclusion of the reacting flow and feedback to the fire are two particularly important and complicating challenges.

10.5 Non-Premixed/Diffusion Flame Shape

Both heat transfer and emissions work may benefit from predicting flame length. Non-premixed flame lengths for enclosed laminar diffusion flames, with similar inputs as those provided by the model here, have been predicted with significant assumptions (steady, 1-D flow, etc) by Roper [23] and Roper et al. [24], although much higher flow rates and unsteady behavior must be considered for biomass cook stoves applications. The unsteady flame shape can likely be studied numerically using computational fluid dynamics with a probability density mixture fraction and large eddy simulation turbulence models. Expected accuracy and applications are unknown at this point.

10.6 Loss Coefficient

Some exploration into the loss coefficient has been made here. Theory and literature based predictions have been compared to a numerical solution using computational fluid dynamics as well as experimental results. The three are in relatively good agreement. Flow dependence has been noted, resulting in an inherent deviation from the initially assumed constant value. However, for the necessary accuracy of this

study a constant loss coefficient has been shown to produce acceptable results. Loss coefficient analysis thus far (other than the experimentally observed value), have been for non-reacting flow. The effect of the reacting flow is currently unknown, but it is thought that a reduced loss coefficient may result.

10.7 Application to other Stove/Fuel Configurations

The stove flow model has been developed using a wood burning rocket elbow stove. The model is likely applicable to other wood burning natural convection chimney stoves with little modification. Some work developing loss coefficients for other stove geometries may be necessary. Stoves without chimney effect driven buoyant flow may not allow for ready application (their design may be informed nonetheless). For restrictive or porous fuel beds such as charcoal, chimney effect driven natural convection may no longer be an important determining factor, and future work would be necessary to explore possible applications. Fan assisted flow, perhaps in a gasifier stove, can likely be included into the model easily, by the addition of the fan pressure difference to that of the chimney effect in Eq. (3).

The relationship of the initially observed emissions trends to other fuel types is unknown. For primarily non-premixed/diffusion flames, these trends may provide some insight. For fuels with dominantly surface combustion, the emissions discussion herein is likely not applicable.

10.8 Acknowledgment and Thank You

This work has been supported by the Colorado State University Engines and Energy Conversion Laboratory, Envirofit International, and the Shell Foundation's Breathing Space Program. For your help, expertise, and advice, I would like to especially thank,

A Non-Constant Specific Heat and Moisture Content Effects

A constant specific heat value taken at an average temperature is assumed for Chapter 2.1 heat addition model derivation. As described, the piecewise polynomial results of Kee et al. [16] can also be used to calculate specific heat values for varying temperature. The piecewise polynomial was incorporated into the iterative solver, and is shown in Appendix C Matlab® code, although commented out. Model predicted mass flow rate and temperature results with the inclusion of the piecewise polynomial are shown in Figure 34 with comparison to the constant specific heat results of Chapter 3.
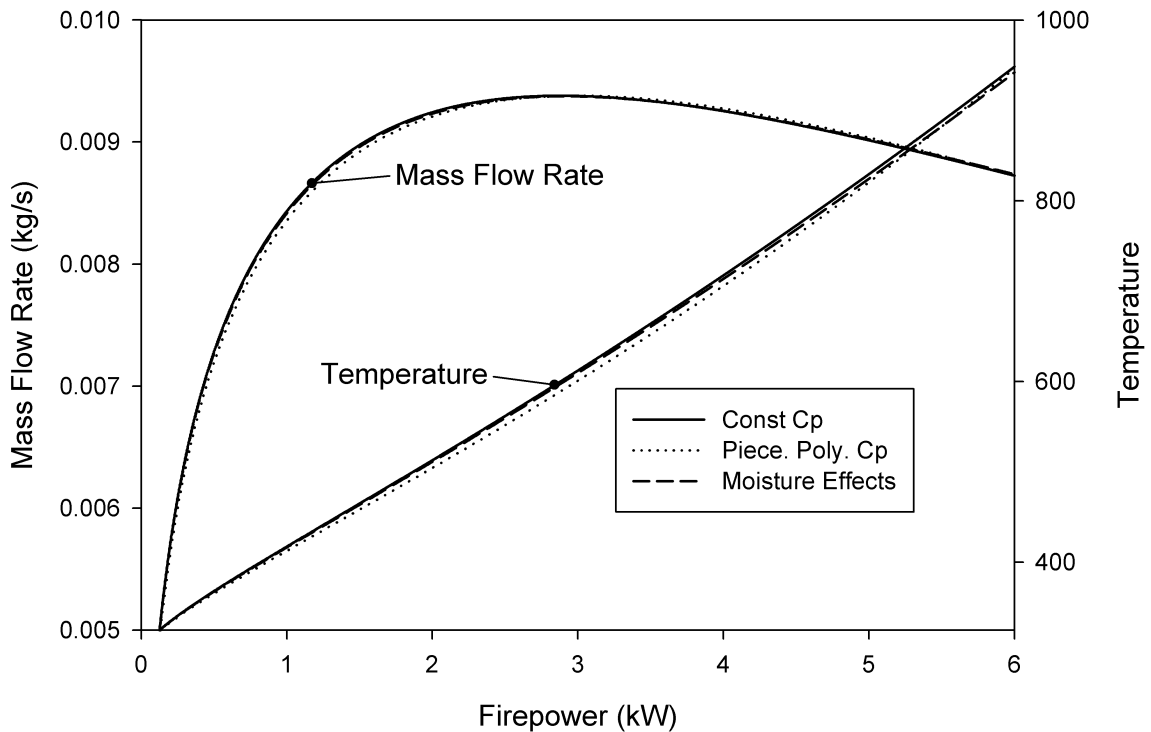

Figure 34: Predicted mass flow rate and temperature behavior for piecewise polynomial specific heat and moisture content effects with comparison to Chapter 3 results.

The resulting error is observed to be relatively small, and the neglect these effects in Chapter 2.1 is shown to be justifiable. Note that if a specific heat is taken at a the

low or high temperature instead of an average value, the resulting error will be more significant and the average value should be used.

Previously neglected fuel moisture content effects will now be examined. Using the gross heating value (GHV), the energy lost to vaporize fuel moisture content can is already accounted for. The effect can also be accounted for by first calculating the mass or molar rate of vaporization from the mass burn rate of fuel and an assumed moisture content. Multiplied this rate by the heat of vaporization, the consumed energy is determined, and is then subtracted from the lower heating value (LHV) of the fuel.

In either case, once vaporized the moisture also consumes additional combustion heat as it is raised to the hot flow temperature. This energy can be accounted for using a piecewise polynomial (as already described for air)to calculate the specific heat of water vapor with varying temperature. Including the lost combustion heat for vaporization and further vapor heating into the iterative model solver, the resulting mass flow rate and temperature curves are shown for comparison in Figure 34 as well. As with the non-constant specific heat, the effect is relatively small, and their neglect in Chapter 2.4 is shown to be justified.

B   Chimney Effect Derivation Details

The Chapter 2.2 chimney effect derivation has skipped some rather simple, but important steps. The detailed steps for converting the density ratio to a corresponding temperature ratio will now be shown. Starting with Eq. (7) from Chapter 2.2 as repeated below in Eq. (69).

$$\dot{V}_2 = A\sqrt{2gh\left(\frac{\rho_{Amb} - \rho_H}{\rho_H}\right)} \tag{69}$$

The ideal gas law is given in Eq. (70) and is substituted into Eq. (69) to give Eq. (71).

$$\rho_H = \frac{P}{R_s T_H} \tag{70}$$

$$\dot{V}_2 = A\sqrt{2gh\left(\frac{\frac{P}{R_s T_{Amb}} - \frac{P}{R_s T_H}}{\frac{P}{R_s T_H}}\right)} \tag{71}$$

The difference inside the parenthesis can be simplified after several steps to the form of Eq. (72).

$$A\sqrt{2gh\left(\frac{\frac{P}{R_s T_{Amb}} - \frac{P}{R_s T_H}}{\frac{P}{R_s T_H}}\right)} \;=\; A\sqrt{2gh\left(\frac{\frac{1}{T_{Amb}} - \frac{1}{T_H}}{\frac{1}{T_H}}\right)}$$

$$= A\sqrt{2gh\left(\frac{\frac{1}{T_{Amb}} - \frac{1}{T_H}}{\frac{1}{T_H}}\right)} \;=\; A\sqrt{2gh\left(\frac{T_H}{T_{Amb}} - \frac{T_H}{T_H}\right)}$$

$$= A\sqrt{2gh\left(\frac{T_H}{T_{Amb}} - 1\right)} \;=\; A\sqrt{2gh\left(\frac{T_H}{T_{Amb}} - 1\right)}$$

$$= A\sqrt{2gh\left(\frac{T_H}{T_{Amb}} - \frac{T_{Amb}}{T_{Amb}}\right)} \;=\; A\sqrt{2gh\left(\frac{T_H - T_{Amb}}{T_{Amb}}\right)} \tag{72}$$

With the form of Eq. (72), solving for the volumetric flow rate yields the same form as Eq. (8). Multiplying by the density and substituting with the ideal gas law of Eq. (70) the mass flow rate previously determined mass flow rate of Eq. (8).

C Chapter 2.4 Dimensional System Matlab Code

The Matlab® code used to solve the dimensional system of equations summarized in Chapter 2.4 is shown below. A function is defined to iteratively solve the system from model inputs. A script is then used to sweep through a firepower range of interest using the iterative solver function. The script is shown first:

```
clc
clear all
close all
format short e

h=0.21; %m
r=0.050; %m
A=pi*(r^2);
Coeff_CE=0.5; %Loss Coeff
%Coeff_HT=1; %Heat Transfer Loss Coefficient

Q_dotRange=[50 9500]; %Set firepower range of interest
steps=149;
stepsize=(Q_dotRange(2)-Q_dotRange(1))/steps;

T_Hguess=600;

for i=1:steps+1 %firepowersweep

Q_dot=Q_dotRange(1)+stepsize*(i-1);

%run iterative solver
[m_dot,V_dot,T_H,EAR_W,EAR_C,PO2_W,PO2_C]
        = ChimneyFlow_V5( Q_dot,h,A,Coeff_CE,Coeff_HT,T_Hguess );

%Store solver results
FPS(i,1)=Q_dot/1000;
FPS(i,2)=m_dot;
FPS(i,3)=T_H;
FPS(i,4)=EAR_W;
FPS(i,5)=PO2_W;

T_Hguess=T_H;

end %increment to next firepower step
```

...followed by the iterative solver function:

```
function [m_dot,V_dot,T_H,EAR_W,EAR_C,PO2_W,PO2_C]
        = ChimneyFlow_V5( Q_dot,h,A,Coeff_CE,Coeff_HT,T_Hguess )

%constant inputs
```

```
P=101325; %Pa=N/m^2
R_s=287; %J/kg-K
g=9.81; %m/s^2
c_p=1150; %J/kg-K
T_C=300; %K
HOC_W=1.8280e7; %J/kg


%Wood Fuel Composition CxHyOz
X=4.4;
Y=6.3;
Z=2.5;
MW_W=12*X+1*Y+16*Z; %kg/kgmol
b_stoich=(4*X+Y-2*Z)/4;
AFR_W_Stoich=(b_stoich*32+3.76*b_stoich*28)/MW_W; %Stoich Air/Fuel Ratio


%%%% values for c_p piecewise polynomial 100-1000K if used %%%
%A1=1161.482;
%A2=-2.368819;
%A3=0.01485511;
%A4=-5.034909e-5;
%A5=9.928569e-8;
%A6=-1.111097e-10;
%A7=6.540196e-14;
%A8=-1.573588e-17;


%%%% values for c_p piecewise polynomial 100-1000K if used %%%
%C1=-7069.814;
%C2=33.70605;
%C3=-0.05812759;
%C4=5.421615e-05;
%C5=-2.936679e-8;
%C6=9.237533e-12;
%C7=-1.565553e-15;
%C8=1.112335e-19;


Error=1;
while (Error>1e-6) %iterative solver, check error

m_dot=(Coeff_CE*A*P/R_s)*(1/T_Hguess)*sqrt(2*g*h*(T_Hguess-T_C)/T_C)


%%%% for piecewise polynomial (no constant) specific heat %%%


%if T_Hguess<=1000
%    T_C_enthalpy=A1*T_C+A2*T_C^2/2+A3*T_C^3/3+A4*T_C^4/4
%         +A5*T_C^5/5+A6*T_C^6/6+A7*T_C^7/7+A8*T_C^8/8;
%    T_H=fzero(@(T_H)m_dot*(A1*T_H+A2*T_H^2/2+A3*T_H^3/3
%         +A4*T_H^4/4+A5*T_H^5/5+A6*T_H^6/6+A7*T_H^7/7
%             +A8*T_H^8/8-T_C_enthalpy)-Q_dot*Coeff_HT,T_Hguess);
%else
%    T_C_enthalpy=A1*T_C+A2*T_C^2/2+A3*T_C^3/3+A4*T_C^4/4
%                    +A5*T_C^5/5+A6*T_C^6/6+A7*T_C^7/7+A8*T_C^8/8;
%    T_1000=1000;
%    T_1000_enthalpy=A1*T_1000+A2*T_1000^2/2+A3*T_1000^3/3
%         +A4*T_1000^4/4+A5*T_1000^5/5+A6*T_1000^6/6+A7*T_1000^7/7+A8*T_1000^8/8;
%    T_1000C_enthalpy=C1*T_1000+C2*T_1000^2/2+C3*T_1000^3/3
%         +C4*T_1000^4/4+C5*T_1000^5/5+C6*T_1000^6/6+C7*T_1000^7/7+C8*T_1000^8/8;
%    T_H=fzero(@(T_H)m_dot*(C1*T_H+C2*T_H^2/2+C3*T_H^3/3+C4*T_H^4/4
%         +C5*T_H^5/5+C6*T_H^6/6+C7*T_H^7/7+C8*T_H^8/8-T_1000C_enthalpy
%             +T_1000_enthalpy-T_C_enthalpy)-Q_dot*Coeff_HT,T_Hguess)
```

```
%end

%%% for constant specific heat %%%

delta_T=Q_dot/m_dotGuess/c_p;
T_H=T_C+delta_T;

Error=abs(T_H-T_Hguess); %calculate error
T_Hguess=T_H;

end

m_dot_wood=Q_dot/HOC_W; % kg/s of wood
m_dot_O2=m_dot*0.21; %kg/s of O2

phi_wood=AFR_W_Stoich/(m_dot/m_dot_wood); %Equivalence ratio

EAR_W=100*(1-phi_wood)/phi_wood; %Excess air ratio

b=m_dot/137.28;
a_wood=m_dot_wood/MW_W;
PO2_W=100*(a_wood*Z+2*b-2*a_wood*X-0.5*a_wood*Y)
/(0.5*a_wood*Y+a_wood*Z+9.52*b); %Predicted flue gas %O2

end
```

D   Chapter 7.2 Dimensionless System Matlab Code

The Matlab® code used to solve the dimensionless system of equations summarized in Chapter 7 is shown below. As in the Apendix C dimensional code, a function is defined to solve the iterative system for model inputs, and a script is used to sweep through a firepower range of interest using the solver function. The script is shown first:

```
clc
clear all
close all
format short e

%constant inputs
h=0.21; %m
r=0.05; %m
A=pi*(r^2);
g=9.81; %m/s^2
R_s=287; %J/kg-K
P=101325; %Pa=N/m^2
T_C=300; %K
rho_knot=P/R_s/T_C;
HV=18280000; %J/kg
c_p=1063; %J/kg-K
LC=0.5
```

```matlab
Q_dotRange=[50 6000]; %Set firepower range of interest
steps=149;
stepsize=(Q_dotRange(2)-Q_dotRange(1))/steps;

for i=1:steps+1 %iterate through firepower range

Q_dot=Q_dotRange(1)+stepsize*(i-1);

%convert to dimensionless firepower
mF_dot=Q_dot/HV;
mF_dot_Star=mF_dot/(LC*A*rho_knot*sqrt(g*h));
HV_Star=HV/c_p/T_C

%run dimensionless iterative solver
[mA_dot_Star,T_Star,Phi] = DimLessChimneyFlow( mF_dot_Star,HV_Star );

%store dimensionless solver results
FPS(i,1)=mF_dot_Star*HV_Star;
FPS(i,2)=mA_dot_Star;
FPS(i,3)=T_Star;
FPS(i,4)=Phi;

end %iterate to next firepower step
```

...followed by the iterative solver function:

```matlab
function [mA_dot_Star,T_Star,Phi] = DimLessChimneyFlow( mF_dot_Star,HV_Star )

T_C=300;
T_H_Guess=500;
T_Star_Guess=(T_H_Guess-T_C)/T_C; %convert to dimensionless initial temp value
AFR_Stoich=6.5454;

Error=1;
while (Error>1e-6) %iterative sovler, check error

    mA_dot_Star=sqrt(2*T_Star_Guess)/(T_Star_Guess+1);

    T_Star=HV_Star*mF_dot_Star/mA_dot_Star;
    %Q_dot_Star/m_dot_Star

    Error=abs(T_Star-T_Star_Guess) %calculate error
    T_Star_Guess=T_Star;

end

AFR=mA_dot_Star/mF_dot_Star;
Phi=AFR_Stoich/AFR;
T_Star;
mA_dot_Star;
```

References

[1] Sam Baldwin, Howard Geller, Gautam Dutt, and N. H. Ravindranath. Improved woodbunning cookstoves: Signs of success. *Ambio*, 14(4/5):280–287, 1985. ISSN 00447447. URL http://www.jstor.org/stable/4313163.

[2] S.F. Baldwin. *Biomass stoves: Engineering design, development and dissemination*. PhD thesis, Center For Energy and Environmental Studies Princeton University, Princeton, New Jersey 08544 USA, 1987.

[3] Douglas F. Barnes, Keith Openshaw, Kirk R. Smith, and Robert van der Plas. The design and diffusion of improved cooking stoves. *The World Bank Research Observer*, 8(2):119–141, July 1993. ISSN 02573032. URL http://www.jstor.org/stable/3986529.

[4] Nigel Bruce, Rogelio Perez-Padilla, and Rachel Albalak. Indoor air pollution in developing countries: a major environmental and public health challenge. Technical Report 78(9), Bull World Health Organ, 2000. URL http://www.scielosp.org/scielo.php?script=sci_arttext&pid=S0042-96862000000900004&lng=en.

[5] Mark Bryden, Dean Still, Peter Scott, Geoff Hoffa, Damon Ogle, Rob Bailis, and Ken Goyer. Design principles for wood burning cook stoves. Technical report, Aprovecho Research Center, 80574 Hazelton Road, Cottage Grove, Oregon 97424, 2005.

[6] Yunus A. Cengel and John M Cimbala. *Fluid mechanics: fundamentals and applications*. McGraw Hill Higher Education, 2006. ISBN 0-07-247236-7.

[7] Ajay Chatterjee and L. J. Deviprasath. A one-equation turbulence model for aerodynamic flows. Technical Report AIAA-92-0439, American Institute of Aeronautics and Astronautics, 1992.

[8] H. W. de Koning, K. R. Smith, and J. M. Last. Biomass fuel combustion and health. *Bulletin ofthe WorldHealth Organization*, 63(1):11 – 26, 1985. URL http://www.ncbi.nlm.nih.gov/pmc/articles/PMC2536350/pdf/bullwho00084-0024.pdf.

[9] Directors and Senior Associates of the PM Centers Headquartered at UCLA. A mid-course (2 1/2 year) report of status, progress, and plans. Technical report, The EPAs Particulate Matter (PM) Health Effects Research Centers Program, 2002.

[10] M F Edwards, M S M Jadallah, and R Smith. Head losses in pipe fittings at low reynolds numbers. *Chemical Engineering Reasearch and Design*, 63:43–50, 1985. ISSN 0263-8762.

[11] Michael Frenklach. Reaction mechanism of soot formation in flames. *Physical Chemistry Chemical Physics*, 4:20282037, Febuary 2002. doi: 10.1039/b110045a. URL http://www.rsc.org/delivery/_ArticleLinking/DisplayArticleForFree.cfm?doi=b110045a&JournalCode=CP.

[12] Andy Haines, Anthony J McMichael, Kirk R Smith, Ian Roberts, James Woodcock, Anil Markandya, Ben G Armstrong, Diarmid Campbell-Lendrum, Alan D Dangour, Michael Davies, Nigel Bruce, Cathryn Tonne, Mark Barrett, and Paul Wilkinson. Public health benefits of strategies to reduce greenhouse-gas emissions: overview and implications for policy makers. *The Lancet*, 374(9707):2104 – 2114, 2010. ISSN 0140-6736. doi: DOI: 10.1016/S0140-6736(09)61759-1. URL http://www.sciencedirect.com/science/article/B6T1B-4XSTPDR-B/2/a228dee2ef027d9ad940cb5925b55e12.

[13] M.V. Heitor and A.L.N. Moreira. Thermocouples and sample probes for combustion studies. *Progress in Energy and Combustion Science*, 19(3):259 – 278, 1993. ISSN 0360-1285. doi: DOI:10.1016/0360-1285(93)90017-9. URL http://www.sciencedirect.com/science/article/B6V3W-497BCKX-94/2/9358c4b23a1d9a86f0d4677db577ce07.

[14] Nordica A. Hudelson, K.M. Bryden, and Dean Still. Global modeling and testing of rocket stove operating variations. Technical report, Aprovecho Research Center and Department of Mechanical Engineering,Iowa State University, 80574 Hazelton Road, Cottage Grove, Oregon 97424, No Date.

[15] James J. Jetter and Peter Kariher. Solid-fuel household cook stoves: Characterization of performance and emissions. *Biomass and Bioenergy*, 33(2):294 – 305, 2009. ISSN 0961-9534. doi: DOI:10.1016/j.biombioe.2008.05.014. URL http://www.sciencedirect.com/science/article/B6V22-4T8H38B-1/2/6e5ec727a3ce478944ab71c5010e1409.

[16] R.J. Kee, F.M. Rupley, and J.A. Miller. The chemkin thermodynamic data base. Technical Report SAND-87-8215B, Sandia National Labs., Livermore, CA (USA), march 1990.

[17] J.H. Kent and H.Gg. Wagner. Why do diffusion flames emit smoke. *Combustion Science and Technology*, 41(5 - 6):245 – 269, november 1984. doi: 10.1080/00102208408923834.

[18] Tuyeni Heita Mwampamba. Has the woodfuel crisis returned? urban charcoal consumption in tanzania and its implications to present and future forest availability. *Energy Policy*, 35(8):4221 – 4234, 2007. ISSN 0301-4215. doi: DOI:10.1016/j.enpol.2007.02.010. URL http://www.sciencedirect.com/science/article/B6V2W-4NH6NFF-1/2/e3248896c6aa18a33cadd252d8b640dd.

[19] L. P. Naeher, M. Brauer, M. Lipsett, J. T. Zelikoff, C. D. Simpson, and J. Q. Koenig K. R. Smith. Woodsmoke health effects: a review. *Inhalation Toxicology*, 19(1):67 – 106, 2007. ISSN 0895-8378. doi: DOI:10.1080/08958370600985875. URL http://ehs.sph.berkeley.edu/krsmith/publications/2006%20pubs/JIT%20Woodsmoke2.pdf.

[20] P. J. Oliveira, F. T. Pinho, and A. Schulte. A general correlation for the local loss coefficient in newtonian axisymmetric sudden expansions. *International Journal of Heat and Fluid Flow*, 19(6):655 – 660, 1998. ISSN 0142-727X. doi: DOI:10.1016/S0142-727X(98)10037-1. URL http://www.sciencedirect.com/science/article/B6V3G-3V54R6H-9/2/996bd12b0ba10da3774a41bb765060bf.

[21] J. A. Raub and V. A. Benignus. Carbon monoxide and the nervous system. *Neuroscience and Biobehavioral Reviews*, 26(8):925 – 940, 2002. ISSN 0149-7634. doi: DOI:10.1016/S0149-7634(03)00002-2. URL http://www.sciencedirect.com/science/article/B6T0J-482G67R-3/2/a610db2c37cf65ec34b323434c849764.

[22] F. G. Roper. Soot escape from diffusion flames: A comparison of recent work in this field. *Combustion Science and Technology*, 40(5 - 6):323 – 329, 1984. doi: 10.1080/00102208408923816. URL http://www.informaworld.com/smpp/content~db=all~content=a778731127~tab=citation.

[23] F.G. Roper. The prediction of laminar jet diffusion flame sizes: Part i. theoretical model. *Combustion and Flame*, 29:219 – 226, 1977. ISSN 0010-2180. doi: DOI:10.1016/0010-2180(77)90112-2. URL http://www.sciencedirect.com/science/article/B6V2B-497SDH9-9N/2/6ecb89dc540fa391994dedb2929d716f.

[24] F.G. Roper, C. Smith, and A.C. Cunningham. The prediction of laminar jet diffusion flame sizes: Part ii. experimental verification. *Combustion and Flame*, 29:227 – 234, 1977. ISSN 0010-2180. doi: DOI:10.1016/0010-2180(77)90113-4. URL http://www.sciencedirect.com/science/article/B6V2B-497SDH9-9P/2/68e242eefcf4d51262f20387d81ebe50.

[25] Peter Scott. Updated basic stove design. Web, 2003. URL http://stoves.bioenergylists.org/stovesdoc/Scott/rocket/updated%20basic%20stove%20design.pdf.

[26] Kirk R. Smith. Dialectics of improved stoves. *Economic and Political Weekly*, 24(10):517–522, 1989. ISSN 00129976. URL http://www.jstor.org/stable/4394497.

[27] Kirk R. Smith. Health, energy, and greenhouse-gas impacts of biomass combustion in household stoves. *Energy for Sustainable Development*, 1(4):23–29, 1994. ISSN 0973-0826. doi: DOI: 10.1016/S0973-0826(08)60067-8. URL `http://www.sciencedirect.com/science/article/B94T4-4VC2G5V-9/2/630493564774067b5b408ad2705b437a`.

[28] Kirk R. Smith, Michael G. Apte, Ma Yuqing, Wathana Wongsekiarttirat, and Ashwini Kulkarni. Air pollution and the energy ladder in asian cities. *Energy*, 19(5):587 – 600, 1994. ISSN 0360-5442. doi: DOI:10.1016/0360-5442(94)90054-X. URL `http://www.sciencedirect.com/science/article/B6V2S-498M444-5S/2/c5cf6abcc2a4be03cb29039c27432114`.

[29] Kirk R. Smith, Sumi Mehta, and Mirjam Maeusezahl-Feuz. The burden of disease from indoor air pollution in developing countries: comparison of estimates. *International Journal of Hygiene and Environmental Health*, 206(4-5):279–289, 2003. ISSN 1438-4639. doi: DOI:10.1078/1438-4639-00224. URL `http://www.sciencedirect.com/science/article/B7GVY-4DS75H1-7C/2/0523b72507d04000c3ba0b4ae602df3e`.

[30] D.A. Tillman. *Wood as an energy resource.* Academic Press Inc., New York, NY, January 1979.

[31] C. Venkataraman, G. Habib, A. Eiguren-Fernandez, A. H. Miguel, and S. K. Friedlander. Residential biofuels in south asia: Carbonaceous aerosol emissions and climate impacts. *Science*, 307(5714):1454–1456, March 2005. doi: DOI:10.1126/science.1104359. URL `http://www.sciencemag.org/cgi/content/abstract/307/5714/1454`.

[32] R. Viskanta. Heat transfer to impinging isothermal gas and flame jets. *Experimental Thermal and Fluid Science*, 6(2):111 – 134, 1993. ISSN 0894-1777. doi: DOI:10.1016/0894-1777(93)90022-B. URL `http://www.sciencedirect.com/science/article/B6V34-48188SJ-1G/2/eb0a2de08e4c65c3b9ce2e340c73c30a`.